



The effects of internal forces and membrane heterogeneity on three-dimensional cell shapes

Jay A. Stotsky¹ · Hans G. Othmer¹ 

Received: 2 March 2022 / Revised: 7 November 2022 / Accepted: 9 November 2022 /
Published online: 24 November 2022

© The Author(s), under exclusive licence to Springer-Verlag GmbH Germany, part of Springer Nature 2022

Abstract

The shape of cells and the control thereof plays a central role in a variety of cellular processes, including endo- and exocytosis, cell division and cell movement. Intra- and extracellular forces control the shapes, and while the shape changes in some processes such as exocytosis are intracellularly-controlled and localized in the cell, movement requires force transmission to the environment, and the feedback from it can affect the cell shape and mode of movement used. The shape of a cell is determined by its cytoskeleton (CSK), and thus shape changes involved in various processes involve controlled remodeling of the CSK. While much is known about individual components involved in these processes, an integrated understanding of how intra- and extracellular signals are coupled to the control of the mechanical changes involved is not at hand for any of them. As a first step toward understanding the interaction between intracellular forces imposed on the membrane and cell shape, we investigate the role of distributed surrogates for cortical forces in producing the observed three-dimensional shapes. We show how different balances of applied forces lead to such shapes, that there are different routes to the same end state, and that state transitions between axisymmetric shapes need not all be axisymmetric. Examples of the force distributions that lead to protrusions are given, and the shape changes induced by adhesion of a cell to a surface are studied. The results provide a reference framework for developing detailed models of intracellular force distributions observed experimentally, and provide a basis for studying how movement of a cell in a tissue or fluid is influenced by its shape.

Dedicated to Avner Friedman on his 90th birthday. Avner has made very significant contributions to mathematical biology via his founding of the Mathematical Biosciences Institute at Ohio State University and his mentorship of many researchers.

✉ Jay A. Stotsky
jstotsky@umn.edu

Hans G. Othmer
othmer@umn.edu

¹ School of Mathematics, University of Minnesota, Minneapolis, MN 100190, USA

Keywords Cell cortex · Helfrich energy · Surface finite element method

Mathematics Subject Classification 92-08 · 92-C17 · 92-C10

1 Introduction

Cell locomotion plays an essential role in both single-cell and multicellular organisms, and movement is a complex process that involves the spatio-temporal control and integration of a number of sub-processes. These include the transduction of chemical or mechanical signals from the environment, intracellular biochemical responses, and translation of the intra- and extracellular signals into a mechanical response. The essential ingredient for motion is that a cell must be able to transmit force to its surroundings, and this can be done in many ways (Paul et al. 2017; Othmer 2018). Some cells use cilia to swim while others simply crawl, but some cells interrogate the environment and adopt the appropriate mode. There are two major modes of individual cell movement of eukaryotic cells, the mesenchymal or crawling mode, which typically involves strong adhesion to a surface, and the amoeboid mode, which involves weaker attachment, and can involve swimming or movement by deformation through tissues (Lämmermann et al. 2008). A summary of the qualitative shapes of both modes and how they depend on the cell's environment is shown in Fig. 1.

Three examples of the diversity of amoeboid movement used by *Dictyoselium discoideum* (Dd) and the shapes that arise during movement are shown in Fig. 2. In one mode cells move by blebbing, which involves cycles of extension of the front and retraction of the rear (Fig. 2a), while in a second they extend rounded protrusions called pseudopodia (Fig. 2b). A third, less-studied mode used by eukaryotic cells involves swimming in a fluid. Barry and Bretscher (2010) showed experimentally that both Dd cells and neutrophils can swim through fluid-filled voids in their environment by propagating protrusions down their body length, as shown in Fig. 2c. This mode has been analyzed using a 2D model and the results give insights into how characteristics of the protrusions, such as their height, affect the swimmer's speed and efficiency (Wang

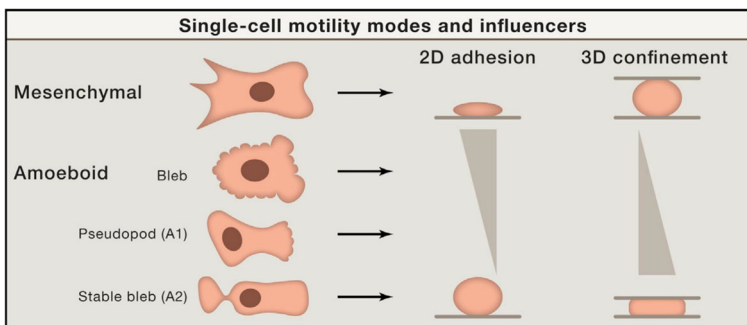
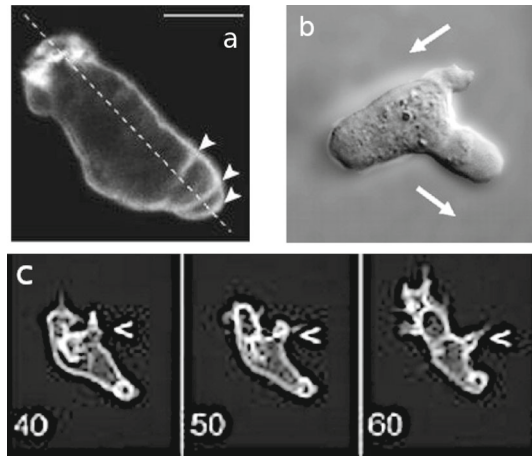


Fig. 1 A summary of the different modes of movement in different environments. From Welch (2015) with permission

Fig. 2 **a** A *Dictyostelium discoideum* (Dd) cell migrating to the lower right by repetitive blebbing. Arrowheads indicate the successive blebs and arcs of the actin cortex. Reproduced with permission from Charras and Paluch (2008). **b** A *Dictyostelium* cell moving by retraction of one pseudopod and extension of another. Reproduced with permission from Zhang et al. (2002). **c** Three snapshots of a swimming *Dictyostelium* cell



and Othmer 2015). The protrusions exhibited in these examples involve deformations of the cell shape that result from localized changes in forces from the CSK, from osmotic effects and from forces from the microenvironment, which may include other cells. These shape changes require forces that must be correctly orchestrated in space and time to produce net motion,

and to understand this orchestration one must couple the intracellular dynamics with the state of the surrounding fluid or tissue microenvironment. Tension in the membrane and the underlying cortex has emerged as an important factor in this orchestration, and these tensions play a very clear role in some cells.

The steady-state shapes of vesicles, red blood cells and other cell types have been studied in great detail, both in the absence of fluid motion and in flows (Seifert et al. 1991; Seifert 1997; Tu and Ou-Yang 2014; Guckenberger and Gekle 2017; Mesarec et al. 2019; Keren et al. 2008; Mogilner and Keren 2009; Lieber et al. 2015). In vesicles, which are closed, self-contained lipid bilayers filled with fluid – in essence a cell without the CSK, the nucleus, and other structures – the intrinsic mechanical forces are the bending forces of the membrane, and computational results for vesicles without interior or exterior fluids lead to a variety of shapes. An example of a phase diagram showing the domains in which various axisymmetric shapes computed in 2D exist as a function of the reduced volume and the spontaneous curvature, both defined later, is shown in Fig. 3a, and a sequence of the shapes along the $C_0 = 0$ line is shown in Fig. 3b, wherein the vertical lines represent discontinuous transitions between the three types of shape.¹ Recent work has extended the free-form shapes of floating vesicles to their shapes when attached to a substrate, again in the axisymmetric case (Raval and Gozdz 2020). Several examples of how the vesicle shape changes as the radius of the circle of attachments to a substrate is increased are shown in Fig. 4.

¹ The prolate and oblate shapes are distinguished by whether the axis of radial symmetry (the height of each shape in Fig. 3b) is shorter or longer than the maximum diameter (the width). Oblate shapes have a maximum diameters that are longer than their axial length, whereas prolate shapes have a longer axial lengths.

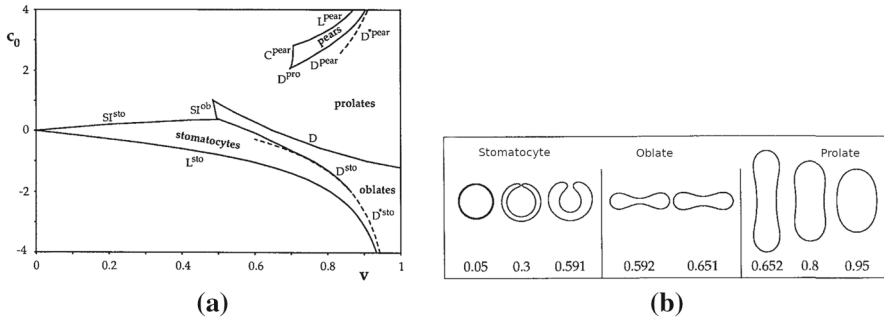


Fig. 3 **a** Phase diagram of the shapes as a function of the reduced volume V and the spontaneous curvature C_0 , both defined later. **b** The qualitative shapes of the vesicles as a function of v along $C_0 = 0$. Modified from Seifert et al. (1991)

Fig. 4 A sequence of shapes for a reduced volume of 0.545 and spontaneous curvature 0. **r** represents the radius of the contact area. Modified from Raval and Gozdz (2020)



The observed cellular shapes shown in Figs. 1 and 2, and the vesicle shapes shown in Fig. 3, raise a number of interesting questions. Firstly, can one predict the balance of forces within a cell needed to produce the various shapes shown in Fig. 2, and to what extent are the shapes fixed by the mechanical feedback from interrogation of the microenvironment of the cell? Secondly, how do forces in the CSK and external forces alter the intrinsic shapes shown in Fig. 3, and how does this affect the movement of cells? Interestingly, some cells cannot move if they are only in contact with the substrate on the ventral side, but will move when confined in a micro-channel (Bergert et al. 2012), which suggests that the intracellular mechanics may be delicately balanced.

The shape of amoeboid cells, which have a less-structured CSK than mesenchymal cells, is mainly determined by the internal forces in the membrane and the forces in the cortex, which implicitly reflect internal CSK forces. As described above, vesicle shapes due only to membrane forces have been widely studied, but little has been done to incorporate cortical forces in models of a cell. A detailed model of the membrane-cortex interaction would be very complex and difficult to analyze, and, as in previous work (Wu et al. 2018; Stotsky and Othmer 2022), we circumvent this difficulty by studying the shapes under various specified force distributions. In essence, we extend earlier work summarized in Fig. 3 by incorporating surrogates for cortical forces in 3D cells that are not necessarily axisymmetric. Some earlier work in this direction is reported in Stotsky and Othmer (2022), and in this paper we extend these results in several directions.

However, the analysis herein is not directed solely toward shapes for cell movement, since the same mathematical techniques apply whenever forces are involved in changing the shape of the membrane. Rather, we focus on the general problem of how the observed shapes of cells, both localized and cell-level, depend on the distribution of forces. Membrane curvature plays a central role in determining the shape, and much

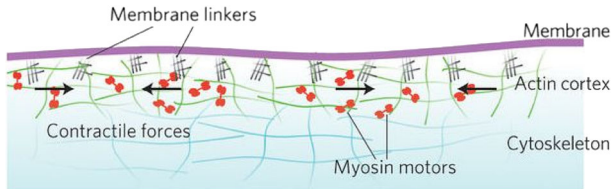
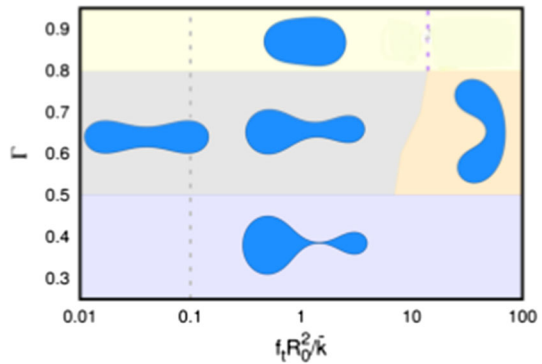


Fig. 5 The plasma membrane (purple) is attached to the actin cortex (green) by linker proteins (black hashes). The cortex is enriched in myosin motors (red), which generate contractile forces. Reproduced with permission from Moendarbary and Charras (2015)

Fig. 6 The effect of a left-to-right gradient of a tangential force on the shape of an axisymmetric cell at various reduced areas (denoted by Γ on y-axis). The normal force, f_n , in these shapes is set to 0. Details of the forces are given later. Reproduced with permission from Wu et al. (2018)



is qualitatively known about how binding of proteins to the membrane can change the local force distribution and hence the curvature that is involved in structures such as filopodia or in tubulation (Stachowiak et al. 2010, 2012; Simunovic et al. 2016a, b; Yuan et al. 2021). An overview of the origins of membrane curvature due to protein binding is given in McMahon and Boucrot (2015), and a review of the physics and the resulting effects on cell shape is given in Mesarec et al. (2021).

We treat the membrane as an elastic medium and the shapes are computed as stationary distributions of the free energy of the membrane, subject to constraints of conserved area and volume, and to the applied forces. The membrane consists of a lipid bilayer ~ 10 nm thick that is attached to a highly-localized component of the CSK called the cortex, which is 200–300 nm thick (Fig. 5). The cortex is comprised of a cross-linked filamentous actin network, embedded with motor proteins and linker proteins that tether the cortex to the membrane, but the connections are dynamic and the cortical actin filaments are continuously turned over by treadmilling (Fritzsche et al. 2016). The cortex can exert both normal and tangential forces on the membrane, but it can also slide tangentially under the membrane (Hochmuth et al. 1996; Dai and Sheetz 1999). It is known that the cortical forces are the primary determinant of cell shape in amoeboid cells (Chugh et al. 2017), and local modulation of cortical mechanics can drive cell deformations during cell division, migration, and tissue morphogenesis (Hawkins et al. 2011; Salbreux et al. 2012; Kapustina et al. 2013; Bovellan et al. 2014). An illustration of the effect of applied tangential forces is shown in Fig. 6.

In many cells these forces generate cell-level flows that are also involved in cell polarization and localization of components involved in shape changes (Ruprecht et al.

2015; Liu et al. 2015). In vivo a cell membrane is subject to dilatation, shear, bending and torsion, but generally only the bending mode is considered when determining stationary vesicle shapes. In rheological terms the membrane-cortex composite exhibits both elastic and viscous responses to stress, but here we are only concerned with the stationary shapes of the cells and thus consider only the elastic component. This is consistent with experimental approaches that focus on measuring membrane tension via aspiration experiments, in which there is no membrane motion (Pontes et al. 2017). The energetics of the elastic response are represented by the Canham-Helfrich (CH) functional described in the following section. The CH free energy only accounts for bending energy and has been widely-used, and in particular is the basis for the shapes shown in Fig. 3. However, vesicles have no cortical layer and no other forces are accounted for in computing their shape. Here we impose both normal and tangential forces as surrogates for the effects of the cortex to shed some light on the role of cortical forces without formulating a detailed model of the interaction between the membrane and the cortex – a more general treatment of fluid–structure interaction for cells immersed in a fluid or tissue is the subject of future work. In the absence of imposed forces the stationary shapes are minimizers of the CH bending energy subject to the area and volume constraints, but in general, imposed forces are not conservative, and we use a virtual work argument to determine the stationary shapes in this case.

In the following section we develop the governing equations and summarize the background concepts for the analysis of surfaces needed throughout. The two main components addressed concern the stationary cell shapes, both in the presence and absence of applied forces, and in Sect. 3 we give a brief description of the numerical methods used in each case. This is followed in Sect. 4 by computational results for the stable shapes that exist in the absence of applied forces, when the bending energy and spatial variations in the bending moduli determine the shapes. The results for constant moduli are compared with the results described above which were obtained using the equations for axisymmetric shapes. We also show results for variable bending moduli and the effects these have on shapes.

In Sects. 5 and 6 we turn to the analysis of shapes under imposed forces. This includes an analysis of the effect of normal and tangential forces alone and in concert. We also include a discussion of the potential effects of normal and tangential forces under various modes of areal constraints. The theoretical results are accompanied by a number of computational results depicting how the stationary shapes vary as the normal force, the tangential force, and the reduced volume vary.

Finally, in Sect. 7, we address how adhesion to a surface can alter the cell shapes. This is done through a simple adhesion model, and suggests that significant shape changes can occur when cells adhere to a substrate. Interestingly, the resulting equilibria are somewhat different than those obtained in Raval and Gozdz (2020), a difference that may be due to differences in how we modeled the cell adhesion, and perhaps, also due to the presence of multiple minimizers of the bending energy, a feature that has been previously observed in Seifert et al. (1991) and Stotsky and Othmer (2022) for free-floating cells.

2 The governing equations

We let $\Omega \subset \mathbb{R}^3$ denote the volume occupied by the cell and let \mathcal{S} denote its boundary. We assume that \mathcal{S} is a smooth, compact, two-manifold without boundary, parameterized by the map $\Phi : D \subset \mathbb{R}^2 \rightarrow \mathcal{S}$, defined so that the position vector \mathbf{x} to any point on the membrane is given by $\mathbf{x} = \mathbf{x}(u^1, u^2)$ for a coordinate pair $(u^1, u^2) \in D$. Let \mathbf{n} denote the outward normal on \mathcal{S} , and define basis vectors on the surface via

$$\mathbf{e}_i = \frac{\partial \mathbf{x}}{\partial u^i} \quad i = 1, 2. \tag{1}$$

In general these are not unit vectors.

The Canham-Helfrich (CH) free energy associated with bending of membranes has the form (Canham 1970; Helfrich 1973; Zhong-Can and Helfrich 1989)

$$\mathcal{E}_B = \int_{\mathcal{S}} \frac{1}{2} k_B (2H + C_0)^2 dS + \int_{\mathcal{S}} k_G K dS. \tag{2}$$

Here c_1 and c_2 are the principal curvatures, $H = -(c_1 + c_2)/2$ is the mean curvature, and $K = c_1 c_2$ is the Gaussian curvature.² C_0 is a phenomenological parameter called the spontaneous curvature, k_B is the bending rigidity or modulus – which may be stress-dependent (Diz-Muñoz et al. 2016), and k_G is the Gaussian rigidity or modulus, which may also vary over the membrane. When k_G is constant, the integral of the Gaussian curvature is constant if Ω does not change topological type under deformation, and the integral can be ignored³.

In addition to the bending energy, which to lowest order is proportional to the square of the local curvature of the membrane in the CH formulation, there are contributions to the free energy corresponding to the work associated with area and volume changes when these are conserved. To account for the work done by any applied forces \mathbf{f} during a deformation, we add the virtual work term $\int_{\mathcal{S}} \mathbf{f} \cdot \delta \mathbf{x} dS$, where $\delta \mathbf{x} = \psi \mathbf{n} + \phi^i \mathbf{e}_i$ is an infinitesimal deformation of the membrane.⁴ Under the constraints of constant surface area A_0 and volume V_0 of the cell, the total free energy takes the form

$$\mathcal{E} = \mathcal{E}_B + \int_{\mathcal{S}} \Lambda (\sqrt{g} - \sqrt{g_0}) du^1 du^2 + P \left(\int_{\Omega} dV - V_0 \right) + \int_{\mathcal{S}} \mathbf{f} \cdot \delta \mathbf{x} dS. \tag{3}$$

Here g is the determinant of the metric tensor \mathbf{g} of the surface, g_0 is its value in a reference configuration in which the area is A_0 , and $P \equiv p_{\text{ext}} - p_{\text{in}}$ is the pressure difference across the membrane, which we assume is constant over the membrane and the internal pressure uniform in the cell. Typically p_{in} is a few hundred pascals higher

² This definition of the mean curvature is predicated on choosing the outward normal as the normal to the surface.

³ By ‘changes in topological type’ we mean that the current configuration of the surface at time t , cannot be mapped to the surface at some previous time $s < t$ via a smooth bijective mapping. This can occur, for instance, if a hole in the surface is formed, or if the surface ruptures into two pieces.

⁴ As discussed in Appendix D, the total work done by applied forces in a finite deformation can be found by integrating along the trajectory of the shape evolution.

than p_{ext} (Salbreux et al. 2012). Here Λ is a Lagrange multiplier for the area constraint. When it can vary over the surface Λ is inside the integral, which reflects the assumption that the area is conserved locally. This applies, for instance, in cases in which a 2–4% stretch leads to rupture of the surface (Boal 2002). If area is only conserved globally but not locally, Λ is a constant. In either case the Lagrange multiplier P for the volume constraint is constant. In still other cases cells have internal reservoirs of membrane and the area constraint is removed.

In the following sections we consider both variable and constant values of Λ . Λ has units of force/length, which defines a surface stress. The constant term PV_0 simply shifts the free energy and can be ignored, since it disappears after the first variation of (3) is taken.

A stable stationary shape of a cell is a minimizer of \mathcal{E} , and thus a solution of $\delta^{(1)}\mathcal{E}/\delta\mathbf{x} = 0$ for any infinitesimal deformation $\delta\mathbf{x}$ of \mathcal{S} . This leads to the following shape equations for the normal and tangential components of the total force on the membrane,⁵

$$\begin{aligned}
 F^n &\equiv -\frac{\delta\mathcal{E}}{\delta\psi} = \left\{ -\Delta_s [k_B (2H + C_0)] - k_B (2H + C_0) (2H^2 - C_0H - 2K) \right. \\
 &\quad \left. - \overline{\Delta}_s k_G + 2\Lambda H - P + f^n \right\} \\
 &\equiv F_p^n(H, K, P, \Lambda, k_B, k_G, u^1, u^2) + f^n \tag{4}
 \end{aligned}$$

$$\begin{aligned}
 F_i^t &\equiv -\frac{\delta\mathcal{E}}{\delta\phi^i} = \left\{ \frac{1}{2} (2H + C_0)^2 \nabla_{s,i} k_B + K \nabla_{s,i} k_G + \nabla_{s,i} \Lambda + f_i^t \right\} \\
 &\equiv F_{i,p}^t(H, K, P, \Lambda, k_B, k_G, u^1, u^2) + f_i^t \quad i = 1, 2 \tag{5}
 \end{aligned}$$

where F_p^n and $F_{i,p}^t$ are the passive forces induced by membrane deformation, and f^n and f_i^t are active forces. Here Δ_s , $\overline{\Delta}_s$ and ∇_s are two forms of the surface Laplacian and gradient, resp., as given in Appendix A, and f^n and f_i^t are the normal and tangential components of the imposed forces. In the normal equation one sees that Λ enters via the term $2\Lambda H$, which couples areal distension to the curvature in the normal component of the total force. In light of how the variation is defined, the resultant forces are defined per unit area. Because eukaryotic cell membranes contain numerous proteins embedded in the lipid bilayer, the spontaneous curvatures are not known for cells, and we will assume $C_0 = 0$ except where otherwise stated.

In addition to control of internally-generated forces, represented here by the imposed forces, another 'lever' that cells have to control their shape is by spatial variation of k_B and k_G . Since k_B scales part of the bending energy, large values of k_B oppose the formation of spherical or cylindrical regions with small radii, and instead favor flatter membranes or saddle structures where $c_1 = -c_2$. Larger, spatially-variable k_G also tends to favor saddle-structures since $K < 0$ reduces the bending energy. However large uniform k_G has no effect unless the topological type of the surface changes, for example, by budding. If $f^n = f_i^t = 0$, we do not expect any new equilibria to

⁵ See Wu et al. (2018) for a derivation of these equations and references to earlier work in Zhong-Can and Helfrich (1989); Capovilla et al. (2003); Yin et al. (2005) and others.

arise in the limit $k_B \rightarrow \infty$ over the entire surface, but rather that the pressure and surface stress simply scale with k_B .

At the other extreme of very small k_B the membrane may become wrinkled with large curvature variations, since the bending force would be comparatively weak compared to other forces in that case. In fact if $k_B = 0$ and k_G is uniform, then in the absence of any other force the stationary shape is arbitrary with no preference for any particular configuration. On the other hand, when k_B is finite and k_G is small and spatially-variable, the k_B -terms simply dominate, leading to stable membrane shapes. As computational results will show later, these remarks, while not rigorous rules, generally tend to hold in practice. Possible effects of local discontinuities in the second order derivatives of k_B and k_G are discussed in Yin et al. (2005), and our results are complementary to theirs in that we consider larger-scale variations in k_B and k_G over the surface.

The case of constant bending and Gaussian rigidities and zero applied forces has been more widely studied, and when k_B and k_G are constant the foregoing variational Eqs. (4) and (5) simplify to

$$F^n = -\frac{\delta \mathcal{E}}{\delta \psi} = -2k_B \Delta_s H - 4k_B H (H^2 - K) + 2\Lambda H - P + f^n \tag{6}$$

$$F_i^t = \nabla_{s,i} \Lambda + f_i^t \quad i = 1, 2. \tag{7}$$

In addition, if the area is only conserved globally, then Λ is a constant and the normal and tangential equations are decoupled. In that case, only the normal equation is required to determine the cell shapes, and the tangential equation is trivial. However, there can be area sources and counter-balancing area sinks in the membrane, and while $f_i^t \neq 0$ it has no impact on the cell shape, it can influence the distribution of these sources and sinks.

To find the stationary shapes for the free energy one could simply set F^n and F_i^t equal to zero and solve the resulting system, the first equation of which is 4th-order in space. This presents significant numerical difficulties (Stotsky and Othmer 2022), but more importantly, since the equations may well have multiple solutions, as already happens in the 2D results shown in Fig. 3, it suggests an alternate approach via Onsager’s variational approach (Doi 2011).

The Onsager approach to the evolution of the state of a system near a stationary state is as follows. Suppose that $X \in R^n$ describes the state of a system and let \mathcal{E} be its free energy. Then assume that the evolution of the state near a steady state is given by the kinetic equation

$$\frac{dX}{dt} = -\Upsilon \nabla_X \mathcal{E}, \tag{8}$$

where Υ is a symmetric, positive-definite matrix and ∇_X is the gradient in the X -frame. This form, or an equivalent form in the entropy, has been used in numerous contexts when a system is near thermodynamic equilibrium. In the present context we will in general start far from stationary shapes and thus there is little physical justification for a linear relation like (8), but since we are only seeking stationary shapes and are

not concerned with the kinetics of the approach to equilibrium, we can use the form in (8). We believe that this approach is reasonable since using the Onsager relations is equivalent to specifying a rule for determining the path a system takes through configuration space as it approaches a minimum energy state. Far from equilibrium, this path may in reality follow a more complex evolution law, but the underlying energy minimizers (the equilibrium shapes) are not affected by this choice. On the other hand, the evolution law could affect the size and shape of the basin of attraction around each minimizer (e.g. sensitivity to initial conditions), however we found that for the axisymmetric case, where the minimizers are known, they were readily obtained given reasonable starting shapes, and no unusual sensitivity to the initial shape was observed.

Thus we define the pseudo-flow

$$\mu_d \frac{d\psi(u^1, u^2)}{d\tau} = F_p^n(H, K, P, \Lambda, k_B, k_G, u^1, u^2) + f^n \tag{9}$$

$$\mu_d \frac{d\phi^i(u^1, u^2)}{d\tau} = F_{i,p}^t(H, K, P, \Lambda, k_B, k_G, u^1, u^2) + f_i^t \quad i = 1, 2 \tag{10}$$

wherein we have chosen Υ to be diagonal. When the cortical forces are incorporated the resulting evolution is no longer a gradient flow for the bending energy alone, and one simply looks for steady states of (9) and (10), which in general are not minimizers of the CH free energy. When the bending moduli are constant the equations simplify considerably, and we consider this case first.

Before solving these equations, we define non-dimensionalized forms. To do so, we introduce characteristic length and time scales $L_0 = 1 \mu\text{m}$ and $T_0 = 1 \text{ s}$, along with a reference energy-level and force density: $\bar{k} = 1 \times 10^{-19} \text{ J}$ and $F_0 = 1 \text{ pN}/\mu\text{m}^2$. Then, define $\mathbf{x}^* = \mathbf{x}/L_0$, $H^* = HL_0$, $k_B^* = k_B/\bar{k}$, $k_G^* = k_G/\bar{k}$, $K^* = KL_0^2$, $\Lambda^* = \Lambda L_0/F_0$, $P^* = P/F_0$, $\mathbf{F}^* = \mathbf{F}/F_0$, $\mu_d^* = \mu_d/(F_0 T_0/L_0)$, c.f. Stotsky and Othmer (2022); Wu et al. (2018). In the following analysis and discussion we drop the star-notation, but will assume the relevant variables are non-dimensionalized unless otherwise stated. A table of commonly used variables along with their dimensional ranges is given in Table 1.

3 Numerical solution of equations

In each case we used the methods developed in Stotsky and Othmer (2022) to solve the shape equation. The basis behind the numerical methods is to develop weak forms of the various forces and then implement a parametric surface finite element method (Dziuk and Elliott 2013) to discretize the weak forces. For curvature forces, it is convenient to consider \mathbf{x} and $\mathbf{H} = 2H\mathbf{n}$ – the surface position, and a vector curvature – as separate variables. They are related via the identity:

$$\Delta_s \mathbf{x} = -\mathbf{H}. \tag{11}$$

Table 1 Commonly used symbols with their dimensional ranges where appropriate. When these quantities are obtained via other literature results, these are listed on the right

Symbol	Definition	Range	References
x	Membrane position	0–10 μm	Alert et al. (2015)
H	Mean curvature	0–10 μm^{-1}	
n	outward normal vector	N/A	
H	$H = 2Hn$	0–10 μm^{-1}	
k_B	Bending rigidity	1–10 $\times 10^{-19}$ J	Alert et al. (2015); Pontes et al. (2013)
k_G	Gaussian bending modulus	1–10 $\times 10^{-19}$ J	
P	Pressure drop, P	1–1000 Pa	Hochmuth (2000)
Λ	(Isotropic) surface stress	0–10 pN μm^{-1}	Hochmuth (2000); Alert et al. (2015); Pontes et al. (2013)
f	Applied force per unit area	1–10 pN μm^{-2}	
Δ_s	Laplace-Beltrami operator	N/A	
∇_s	Surface Gradient	N/A	
S	Set of all x on the surface	N/A	
A	Surface area	10–100 μm^2	
V	Volume enclosed in S	5–30 μm^3	
v	Velocity vector	0–10 $\mu\text{m} \cdot \text{s}^{-1}$	
$E(S)$	Bending energy	50–200 $\times 10^{-19}$ J	
e_x, e_y, e_z	Canonical basis vectors	N/A	
g	Metric determinant	N/A	
u^1, u^2	Surface coordinates	N/A	
C_0	Intrinsic curvature	-3.5–3.5 μm^{-1}	Seifert et al. (1991)
μ_d	Drag coefficient	1 Pa $\cdot \text{s} \cdot \mu\text{m}^{-1}$	
Γ	Reduced volume ^a	0.5–1	

^a For a shape of volume V and surface area A , the reduced volume is computed as $6\sqrt{\pi} \frac{V}{A^{3/2}}$. The factor $6\sqrt{\pi}$ is equal to $A^{3/2}/V$ for a sphere

With this approach, weak forms with favorable numerical properties for computational simulation have been developed (Dziuk 2008; Bonito et al. 2010, 2011).

To begin, we triangulate an initial surface using software packages FELICITY and Jigsaw (Walker 2018; Engwirda 2016). The initial surfaces are chosen to be prolate and oblate spheroids of the form

$$\begin{aligned} \text{Oblate:} \quad & ex^2 + y^2 + z^2 = R^2 \\ \text{Prolate:} \quad & x^2 + ey^2 + ez^2 = R^2 \end{aligned} \tag{12}$$

with $e \geq 1$. By adjusting e the full range of reduced volumes from 0 to 1 can be obtained.

We then approximate the solution of the surface evolution equations by first supposing that within each triangle T_i in a triangulation \mathcal{T} , the solution is a quadratic function of a local parametrization of the surface. This leads to the following finite element space,

$$\mathcal{S} = \left\{ \phi \in C^0(T), \phi_{T_i} \in \mathcal{P}^2(T_i) \right\} \tag{13}$$

consisting of functions ϕ which are C^0 -continuous globally, and locally quadratic when restricted to any particular triangle in \mathcal{T} . With this, we can write a nonlinear weak form of the forces as

$$a(x, \phi) = \int_S \mathbf{F}(x) \cdot \phi dS. \tag{14}$$

As was done previously (Stotsky and Othmer 2022), the bending forces due to the mean-curvature term with $C_0 = 0$ can be written in weak form as

$$\begin{aligned} \int_S \mathbf{F}_B \cdot \phi dS = \int_S \left[\nabla_s \phi : \nabla_s k_B \mathbf{H} - \nabla_s \mathbf{x} \left(\nabla_s \phi + \nabla_s \phi^T \right) : \nabla_s k_B \mathbf{H} \right. \\ \left. + (\nabla_s \cdot \phi) (\nabla_s \cdot k_B \mathbf{H}) + \frac{k_B}{2} |\mathbf{H}|^2 \nabla_s \cdot \phi \right] dS, \end{aligned} \tag{15}$$

and when C_0 is a nonzero constant, this can be modified by replacing \mathbf{H} by $\mathbf{H} + C_0 \mathbf{n}$, except for the last term, which is replaced by $k_B/2(|\mathbf{H}|^2 - C_0^2) \nabla_s \cdot \phi$.

Area conservation and volume conservation are enforced by an approximate method that penalizes deviations in the volume contained in \mathcal{S} , and deviations in the area of each surface triangle. This leads to area conservation forces of the form

$$\int_S \mathbf{F}_A \cdot \phi dS = k_A \int_S \left(\frac{\sqrt{g} - \sqrt{g_0}}{\sqrt{g_0}} \right) \nabla_s \mathbf{x} : \nabla_s \phi dS \tag{16}$$

and the approximate volume conservation is achieved by introducing a force,

$$\int_S \mathbf{F}_V \cdot \phi dS = k_V \left(\frac{V - V_0}{V_0} \right) \int_S \mathbf{n} \cdot \phi dS \tag{17}$$

where V and V_0 are the initial and reference volume of the region contained in S . For sufficiently large k_A and k_V , deviations in the surface area and volume are less than 1% during simulation. Further, while the numerical method has no particular requirements regarding the initial shape, we used spheroidal initial shapes with varying degrees of eccentricity to initialize the simulations with shapes of arbitrary reduced volume. The reference volume V_0 and area A_0 are with regard to these initial shapes. With this approximate method Λ and P can be approximated as $\Lambda = k_A \frac{\sqrt{g} - \sqrt{g_0}}{\sqrt{g_0}}$ and $P = k_V \frac{V - V_0}{V_0}$. In the limit $k_A \rightarrow \infty$ and $k_V \rightarrow \infty$, these values of Λ and P tend towards limiting values which are equal to the values of Λ and P if conservation were enforced exactly.

In some cases, only global surface area conservation applies and then the area conservation force simplifies to ⁶

$$\int_S \mathbf{F}_A \cdot \boldsymbol{\phi} dS = k_A \left(\frac{A - A_0}{A_0} \right) \int_S \nabla_s \mathbf{x} : \nabla_s \boldsymbol{\phi} dS. \tag{18}$$

To compute minimizers of the surface energy functional, we must numerically evolve the pseudo-evolution equations via a time-stepping method. As earlier, the normal and tangential forces associated with variations in \mathcal{E} were associated to the components of normal and tangential flow velocities in Eqs. (9) and (10). This yields an evolution equation of the form

$$\frac{\partial \delta \mathbf{x}}{\partial t} = \mathbf{V} = V^n \mathbf{n} + V_i^t \mathbf{e}^i = \frac{1}{\mu_d} (F^n \mathbf{n} + F_i^t \mathbf{e}^i). \tag{19}$$

We found that solving this system directly after discretization requires extremely small time steps and hence very large computational times. To allow for larger time-steps, we modify this force-velocity relation in a way that yields a monotonically decreasing energy and produces the same final shapes. This is done by treating the membrane as though it were embedded in a viscous fluid as was done in Stotsky and Othmer (2022), which means that (19) can be written in the form

$$\mathbf{V} = \int_S \frac{1}{\mu_d} \mathbf{K}(\mathbf{x} - \mathbf{y}) \mathbf{F}(\mathbf{y}) dS_y \tag{20}$$

where \mathbf{K} is the fundamental solution of the Stokes equation due to a point force,

$$\mathbf{K}(\mathbf{x}) = \frac{1}{8\pi} \left[\mathbf{I} \frac{1}{\|\mathbf{x}\|} + \frac{\mathbf{x} \otimes \mathbf{x}}{\|\mathbf{x}\|^3} \right]$$

⁶ We later argue that global area conservation is an inappropriate constraint in some cases.

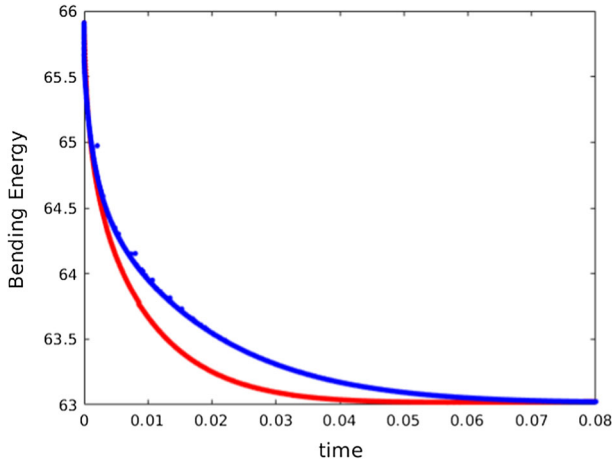


Fig. 7 At each t , the non-dimensional bending energies, \mathcal{E}_B/k_B (with \mathcal{E}_B defined from Eq. (2)) are computed as the membrane, S evolves under the flow the velocities $V = F/\mu_d$ (blue) and $V = (K * F)/\mu_d$ (red) discussed in the text. Time is measured in seconds along the x -axis. It can be seen that both tend towards the same equilibrium energy. On the blue curve, the points that are off the curve correspond to times at which remeshing was done, leading to momentary bumps in the energy

where \otimes indicates the tensor product of two vectors, and I is the 3x3 identity matrix. Given a discretization of the surface, this is approximated as

$$V = \sum_{i=1}^N \frac{1}{\mu_d} K_\delta(x - y_i) F_i dA_i \tag{21}$$

where the $F_i dA_i$ are approximations of the force times a local area at discrete points on the surface, and K_δ is a regularization of K using regularized Stokeslets (Cortez 2001)⁷ A comparison of the evolution of the total energy using the discretization of Eqs. (9) and (10) and the approximate method is shown in Fig. 7. For the results shown in later figures we check the final shape in each case by a short-in-time computation using the discretization of Eqs. (9) and (10).

To evolve the surface using a discretization of (19), we begin with the shape obtained from the first step, and then use a semi-implicit backwards Euler-method. Essentially, in the backwards Euler method certain nonlinear terms are approximated by their values at the previous time-step, whereas linear terms containing the highest order derivatives are solved for implicitly. The full details of this approach are described in Stotsky and Othmer (2022).

In addition, occasional remeshing was required to maintain stability of the simulations after significant deformations occurred. To remesh, a provisional remeshing was first created from the current surface mesh using features of the Jigsaw library. Then,

⁷ A comparison of dimensions in Eqs. (19) and (20) shows that K must be scaled by a factor of $1/L$. This is because μ_d is not a Newtonian viscosity, but rather is a drag coefficient. This is done in the computations.

geometric consistency was enforced by solving

$$\Delta_S \mathbf{x} = -\mathbf{H} \quad (22)$$

on the new mesh as in Bonito et al. (2010).

Typical simulations used several thousand surface points in the triangulations, and time-steps of around $10^{-5} - 10^{-4}$ compared with the characteristic time-scale of the evolution, which is 1 s. Simulations were allowed to run between several thousand up to 25,000 steps and took several hours to a day in most cases. In physical time, these simulations correspond to a range of half a second to several seconds.

4 Shape changes in the absence of applied forces

We first consider the shapes that can be obtained in the absence of any additional forces. The case of constant bending moduli in axisymmetric 2D surfaces has been studied in Seifert et al. (1991) and elsewhere. Thus, as a test of our methods, we reproduce Fig. 8 of Seifert et al. (1991). Starting from the prolate and oblate spheroids described by Eq. (12), the steady-state minimizers of the Helfrich energy are computed from the pseudo-evolution equations. Recall that the reduced volume is a function of the eccentricity e in each case, and as such, distinct prolate and oblate minimizers can be found over a wide-range of reduced volumes.

At any point during the evolution, the bending energy associated with these minimizers is computed as

$$E(S) = \int_S k_B H^2 dS \quad (23)$$

and we set the bending modulus $k_B = 1$ here. The stationary energy levels are of particular interest as they are thought to correspond to shapes that cells (or vesicles) tend to favor. The Gaussian curvature term of the Helfrich energy can be ignored because when k_G is constant, the integral

$$\int_S k_G K dS \quad (24)$$

is a constant so long as the topological type does not change. While the equations used here are non-dimensional, even without that the integrals $\int_S H^2 dS$ and $\int_S K dS$ are dimensionless, and thus the energy levels computed from those terms are scale-independent. In other words, if we were to magnify or shrink the system by an arbitrary factor, the bending energy would remain unchanged, although other energy terms such as the surface stress would certainly be altered.

In Fig. 8 the bending energy as a function of the reduced volume is shown.

Both branches begin with spherical minimizers (with a reduced volume $\Gamma = 1$, spheres are the only possible shape). As Γ is reduced, the prolate branch first yields pill-like shapes followed by spherically-capped cylinders of increasing length. The

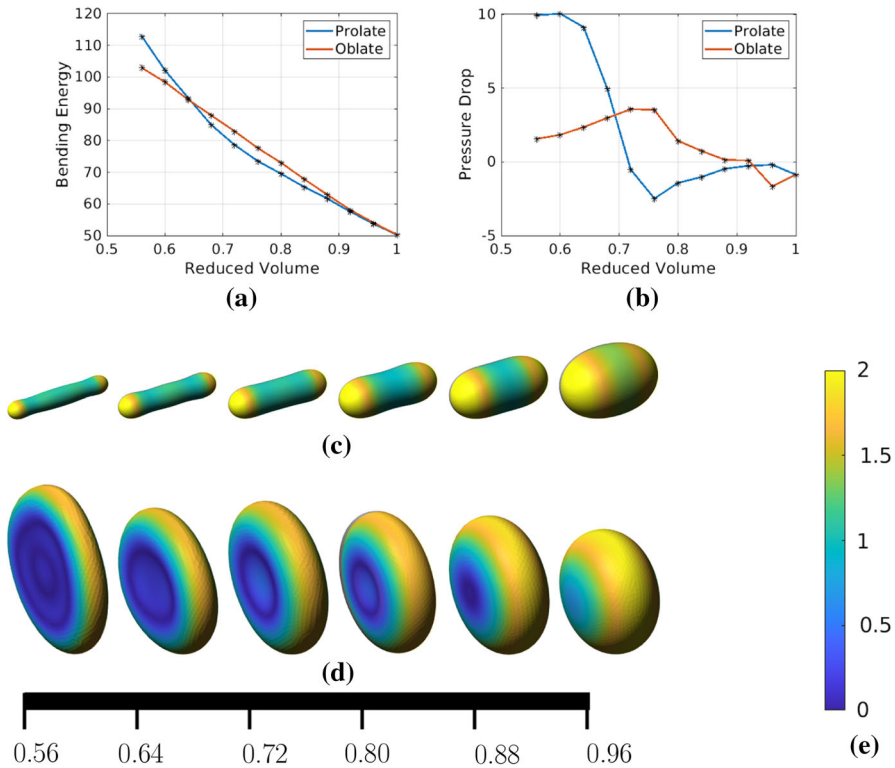


Fig. 8 **a** The bending energy defined in Eq. (23) as a function of reduced volume for oblate (red) and prolate (blue) Helfrich energy minimizers. **b** The pressure drop for the minimizers found in (a). Note that the pressure corresponds to the Lagrange multiplier for volume, which is just a single number, in contrast to a pressure field which may exist in a fluid. **c** Shapes along the prolate branch. **d** Shapes along the oblate branch. **e** The color-scale increases from blue to yellow and indicates the value of $|H|$. Note that to aid visualization, the figures within (c) and (d) are not drawn to scale relative to each other, e.g. at the length scale of our computations, the left-most shape in (c) is several times as long as the right-most shape in (c). The scale-bar at the bottom indicates the reduced volume in (c) and (d). All units in this figure are dimensionless

oblate branch first yields flattened spherical shapes followed by discocyte-like shapes that eventually self-intersect (not shown).

These results closely match those reported in Seifert et al. (1991), where the axisymmetry was assumed *a priori*. As discussed there, although there are multiple local minima, only one shape is a global minimizer. The prolate shapes are the global minimizers for reduced volume levels $\Gamma > 0.651$, and for smaller Γ , oblate shapes are the global minimizers followed by stomatocyte-like shapes for $\Gamma < 0.54$. A phase transition occurs where the energy curves for these branches of minimizers cross, which involves a discontinuity.

It is important to note that this phase-transition reflects mechanics only, but does not take into account the kinetics of the phase-transition, which could be slow if a large amount of deformation or large amount of energy is needed to achieve the transition.

This means that cells may spend a great deal of time in shapes that correspond to local minima rather than global minima.

4.1 Effects of intrinsic curvature

Intrinsic curvature also plays a role in the stationary shapes of vesicles. It can arise from various types of chemical differences in the two sides of the bilayer membrane, or in cases where the fluid on either side of the membrane exhibits different chemical interactions with the membrane.

The effect of intrinsic curvature on cell membranes (rather than vesicle membranes) is less well understood, and specific values for the intrinsic curvature of a cell membrane are not known. However, the ability of various membrane-embedded proteins to locally alter the curvature of the cell membrane suggests that alterations in C_0 may play an important role. Since $2H = -(c_1 + c_2)$, positive C_0 decreases the bending energy $(2H + C_0)^2$ term, and thus facilitates regions of negative mean curvature. These can appear as saddle-like structures, or concave regions of the membrane. In one figure below, a large enough C_0 leads to a dramatic invagination of the membrane. It seems plausible that cells may induce such changes in C_0 in order to achieve endocytosis.

On the other hand, $C_0 < 0$ tends to force H to be positive, and this would be expected to lead to sphere-like subdomains of the membrane connected by thin cylindrical regions. As the cylindrical regions become thin enough, this could potentially lead to topological changes such as budding. Our model does not allow for such topological changes, but we can simulate the shapes that result as the cell approaches such changes.

In our simulations, we consider C_0 to be a uniform constant defined over the entire membrane. With reduced volume $\Gamma = 0.75$ a series of shapes that results from $C_0 \in [-3.5, 4]$ are depicted in Fig. 9.

For large negative C_0 , the shape approaches two spheres touching only at a small neck. As C_0 increases, the shapes smoothly pass through the prolate stationary shape at $C_0 = 0$. At $C_0 \approx 2$, there is a transition to an oblate type shape, and finally above $C_0 \approx 2.5$, the resulting shapes are parachute-like shapes with an increasingly narrow neck region, as depicted in Fig. 10.

For positive C_0 , the cell shape passes through non-axisymmetric intermediaries as it transitions from a prolate shape to an oblate shape. The images in 10 pick up the evolution after an oblate shape has already been reached, but examples of this prolate-to-oblate transition are depicted in Fig. 13 under a different setting. For $C_0 \approx 0$, the shapes remain prolate and axisymmetric as they approach equilibria. The stationary shapes match similar 2D shapes found in Seifert et al. (1991) qualitatively, and our results expand upon earlier results since we compute the full series of intermediary shapes along the path of the pseudo-evolution through configuration space and did not assume axisymmetry at the outset – rather it emerges that the axisymmetric shapes are stable. Unfortunately, as C_0 increases above $C_0 \approx 3$, the neck becomes increasingly narrow, and the current numerical simulations may not sufficiently resolve the shape evolution. As noted above, in living cells, such thin neck-regions may potentially occur during endocytosis or vesicle fission events just prior to topological changes. Thus, the difficulty in resolving such regions may be in part due to numerical difficulties

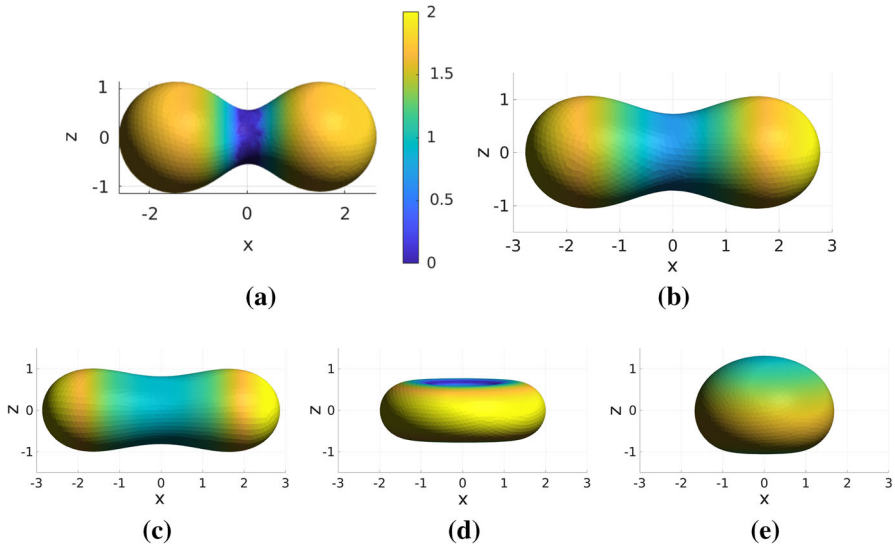
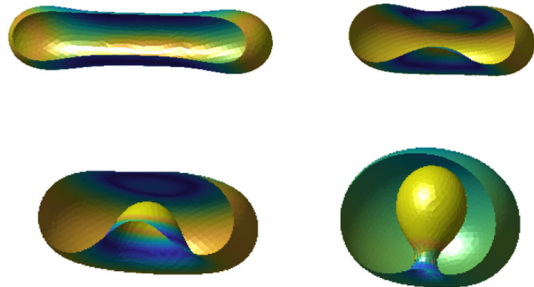


Fig. 9 Depictions of the effect of C_0 on cell shape. From upper left to lower right, $C_0 = -4, -2, 0, 2, 3.5$. Coloration indicates the magnitude of H in each image with the same colorbar as shown on the top left. Note that our values for C_0 are of opposite sign from those reproduced in Figure 3a. Unless stated otherwise, all subsequent figures have coloration reflecting the magnitude of H

Fig. 10 Evolution of the interior region of Fig. 9e. Note the narrow “neck” region connecting the inner part of the surface with the exterior part of the surface



in resolving small length scales, and also due to these simulations reaching the limit of applicability of a model that does not take into account topological changes. Furthermore, biological topological changes sometimes involve specialized enzymes that catalyze the topological change, and including these highly-localized effects would add significantly to the complexity of our model.

5 The effects of normal and tangential forces and variations in the moduli

To simplify the discussion of these effects, we introduce some notation. For any vector field, $\mathbf{v} \in \mathbb{R}^3$ defined in a neighborhood of the surface S , let \mathbf{P} denote the projection

tensor

$$P = I - n \otimes n \tag{25}$$

which projects v onto the tangent space at each point in S . We then decompose the field into normal and tangential components as

$$v = (n \otimes n)v + Pv = v^n + v^t = v^n n + v^{t,i} e_i.$$

First we consider the case of constant bending moduli, in which case Eqs. (4) and (5) can be written as

$$\begin{aligned} n \cdot \mu_d \frac{\partial x}{\partial t} &= F^n = B^n - P + 2\Lambda H + f^n \\ P \cdot \mu_d \frac{\partial x}{\partial t} &= F^t = \nabla_s \Lambda + f^t \end{aligned} \tag{26}$$

where

$$B^n = -2k_B \Delta_s H - 2k_B H (2H^2 - 2K)$$

are the bending forces, which only have a normal component in this case. The derivative $\partial x / \partial t$ is the Lagrangian velocity of a point on the surface, and hence we will write

$$\frac{\partial x}{\partial t} \equiv V = V^n n + PV^t \tag{27}$$

in normal and tangential components. To better understand the effects of the imposed forces, we analyze how, starting from a shape that minimizes the Helfrich energy at a fixed area and volume – hereafter called a CH shape – the application of forces alters the normal and tangential force balances, thereby leading to new shapes.

5.1 Normal forces with global or local area conservation

In certain cells, it has been observed that over short enough time scales, area changes by more than a few percent cause rupture of the membrane (Boal 2002). However, other cells readily add and remove membrane material to create sustained membrane flows. While the full range of behaviors is beyond our current model, we elaborate here two simple cases. In the first, area is locally conserved, and this corresponds to a membrane that is not exchanging mass with the cytosol. In the second case only the global surface area is conserved, which allows for local sources and sinks.

Let us consider the CH force balance, written as

$$\mu_d \frac{\partial \psi}{\partial t} \equiv \mu_d V^n = B^n - P + 2\Lambda H \tag{28}$$

$$\mu_d \frac{\partial \phi^i}{\partial t} \equiv \mu_d V^{i,t} = \nabla_s^i \Lambda \quad i = 1, 2 \tag{29}$$

and determine what occurs when forces are applied. As written, this force balance applies when the area is conserved locally, but when area-conservation is global Λ is constant, and in that case the gradient term vanishes in the tangential equation.

If the tangential force is zero but the normal force is non-zero, the balance equations under global area conservation reduce to

$$\begin{aligned} \mu_d V^n &= B^n - P + 2\Lambda H + f^n \\ \mu_d V^t &= \mathbf{0}. \end{aligned}$$

Thus, when the moduli are constant there is no tangential motion, regardless of the normal forces. We also see that if the surface was a stationary shape prior to force application, *i.e.*, if

$$0 = B^n - P + 2\Lambda H, \tag{30}$$

then if $f^n = \text{const}$ a new steady state is found by adding that same constant to P , but there is no change in shape.

More generally, if a steady shape exists upon force application, then f^n must be balanced by changes in B^n and Λ as well as P . For instance if $f^n = \text{const} \times H$, then changing Λ while leaving P and B^n fixed yields a steady state. More generally, we can write

$$f^n = \left(\frac{\int f^n dS}{\int dS} \right) + \left(\frac{\int f^n H dS}{\int H dS} \right) H + \tilde{f}^n \tag{31}$$

and we can see that adjusting P by the mean-value of f^n , Λ by the H -weighted mean-value of f^n , and B^n by $-\tilde{f}^n$ yields a new equilibrium. Since only changes in B^n lead to changes in the surface shape (at a fixed area and volume), then \tilde{f}^n is the component of the normal force that leads to shape changes whereas the other terms in f^n contribute to pressure and surface stress changes.

Now consider the case with local area conservation with no tangential force, for which

$$\begin{aligned} \mu_d V^n &= B^n - P + 2\Lambda H + f^n \\ \mu_d V^t &= \nabla_s \Lambda. \end{aligned}$$

This suggests that there could be a steady-state tangential flow. However, we note that for a time-independent shape, the normal velocity vanishes and local area conservation implies that $\nabla_s \cdot V^t = 0$ and therefore $\Delta_s \Lambda = 0$. For smooth closed surfaces this implies that Λ is a constant, since

$$0 = - \int_S \Lambda \Delta_s \Lambda dS = \int_S \|\nabla_s \Lambda\|^2 dS \Rightarrow \nabla_s \Lambda = \mathbf{0} \Rightarrow \Lambda = \text{const.}$$

In particular, it must be the same constant as in the global area conservation case.

Thus, upon application of normal forces, local and global area conservation should lead to the same results. However, note that this ignores fluid–structure interaction since we only consider the shape equation. If fluid–structure interaction is included, there is no reason to expect the same results. In particular, if $\int f dS \neq \mathbf{0}$, there will be rigid body motion, and while this has no effect on the force distribution in the shape equations, this could lead to different results with normal and tangential forces acting on the surface when considering fluid–structure interaction.

5.2 Tangential forces with global or local area conservation

Next, consider global area conservation with tangential applied forces. If the normal and tangential components are balanced prior to force application, then we have

$$0 = B^n - P + 2\Lambda H,$$

and a trivial balance in the tangential direction prior to force application because Λ is constant. The normal force balance is unchanged and thus there is no change in shape upon application of tangential forces, but the latter can induce a tangential flow that acts as parallel transport along the tangential force field given by

$$\mu_d \mathbf{V}^t = \mathbf{f}^t. \tag{32}$$

This differs from the case in which local area is conserved, where the tangential force balance is

$$\mu_d \mathbf{V}^t = \nabla_s \Lambda + \mathbf{f}^t. \tag{33}$$

Local area conservation implies that $\nabla_s \cdot \mathbf{V}^t = 0$ when the normal velocity is zero, but the applied force may or may not be solenoidal. If it is, then it follows from (33) that Λ is constant, since $\Delta_s \Lambda = 0$.

The tangential balance can be written as

$$\mathbf{f}^t = \mu_d \mathbf{V}^t - \nabla_s \Lambda \tag{34}$$

and we can identify this with the Hodge decomposition (Renteln 2013) of \mathbf{f}^t into solenoidal and irrotational components (see Appendix B). We can then write

$$\begin{aligned} \nabla_s \times \mathbf{f}^t &= \mu_d \nabla_s \times \mathbf{V}^t = \mu_d \nabla_s \times \nabla_s \times \psi = -\mu_d \Delta_s \psi. \\ \nabla_s \cdot \mathbf{f}^t &= \mu_d \nabla_s \cdot \mathbf{V}^t - \Delta_s \Lambda \end{aligned}$$

where ψ and Λ are uniquely determined due to the orthogonality of the Hodge decomposition (the curl operator on a manifold is discussed in Appendix B). Thus the

application of a non-solenoidal tangential force field yields a variable tension distribution Λ which affects the normal force distribution via the ΛH term in

$$\mu_d V^n = B^n - P + 2\Lambda H. \quad (35)$$

Since ΛH is determined from the tangential force balance, the values of B^n , P and $\mu_d V^n$ must adjust to balance ΛH . In particular, if B^n changes this indicates that the shape changes in response to tangential forces, a phenomenon impossible in the case of global area conservation alone.

5.3 Combined normal and tangential forces

When area is only conserved globally, there are no cross-terms that appear in the normal and tangential balances, and the effects of the normal and tangential forces combine linearly. However, this result is rather uninteresting since tangential forces do not cause shape changes in this case. On the other hand, when area is conserved locally, it is difficult to say much in general since the two balances are coupled by terms involving Λ and depend nonlinearly on the surface shape. Nonetheless, in simulation it is interesting to note that the effects appear not to deviate too much from “linear” behavior in the sense that if one considers a convex combination of a normal and a tangential force, e.g.

$$\mathbf{f} = \beta f^n \mathbf{n} + (1 - \beta) \mathbf{f}^t \quad (36)$$

for $\beta \in (0, 1)$, the steady-state shapes appear to smoothly transition between that observed with $\beta = 0$ (only tangential forces) and $\beta = 1$ (only normal forces) without passing through intermediary configurations that are of a different character. It is also interesting that in some cases, normal and tangential force effects can cancel out leading to relatively little change in the surface shape. That this can occur can be gleaned from the fact that if \mathbf{f}^t is solenoidal, then

$$\nabla_s \cdot \mathbf{f}^t = \Delta_s \Lambda = 0 \Rightarrow \Lambda = \text{const} \quad (37)$$

or if $f^n = -2H\Lambda$ (with constant Λ), then the bending forces (which depend on shape) need not be altered to balance the effect of the tangential forces. Of course, this need not always be the case, and the normal and tangential forces may combine synergistically to yield more extreme shape changes as well.

5.4 Effects of heterogeneous bending moduli

Finally, we consider a qualitative description of the force balances when the moduli vary. With variable k_B or k_G , changes occur to the normal and tangential force balance as compared with constant moduli. To clarify the roles of the bending moduli, we assume that there are no applied forces ($f^n = 0$ and $f_i^t = 0$).

First, the normal bending forces become

$$B^n = -2\Delta_s(k_B H) - 4k_B H(H^2 - K) - \overline{\Delta}_s k_G$$

and there are now tangential forces related to bending,

$$B^t = 2H^2 \nabla_s k_B + K \nabla_s k_G$$

At steady state, with no surface flows, these bending moduli gradients act to set the distribution of Λ , e.g.

$$\mathbf{0} = -\mathbf{B}^t + \nabla_s \Lambda$$

Thus, in the presence of variable bending moduli, Λ is variable even if there are no external forces applied. In particular, we find that

$$\Delta_s \Lambda = \nabla_s \cdot \mathbf{B}^t$$

This variable Λ also shows up in the normal force balance as $2H\Lambda$. This force also acts non-locally since Δ_s^{-1} is a non-local operator.

On the other hand, under global area conservation only, the tangential gradients will lead to a surface flow,

$$\mu_d \mathbf{V}^t = K \nabla_s k_G + 2H^2 \nabla_s k_B. \tag{38}$$

If k_B and k_G are Lagrangian functions, *i.e.*, they are functions of material points on the surface, this surface flow leads to regions of low k_B and k_G expanding, and high k_B and k_G regions shrinking. Given the form of the bending energy, this result is to be expected, since decreasing k_B and k_G will reduce the energy.⁸

6 Shape changes under applied forces

We compute the normal and tangential vectors at each point on the surface and incorporate forces of the form

$$\mathbf{f}^n = f^n(u^1, u^2) \mathbf{n} \tag{39}$$

or

$$\mathbf{f}_i^t = f^t(u^1, u^2) \mathbf{e}_i \tag{40}$$

⁸ In light of this observation, and the fact that tangential forces do not affect the cell shape under global area conservation, we believe that using global area conservation in models of cell shape is problematic. However, since previous works on vesicle shapes often use this approach, and because it is numerically easier to implement than local conservation, we give a description of what occurs here. Subsequent numerical computations use local area conservation.

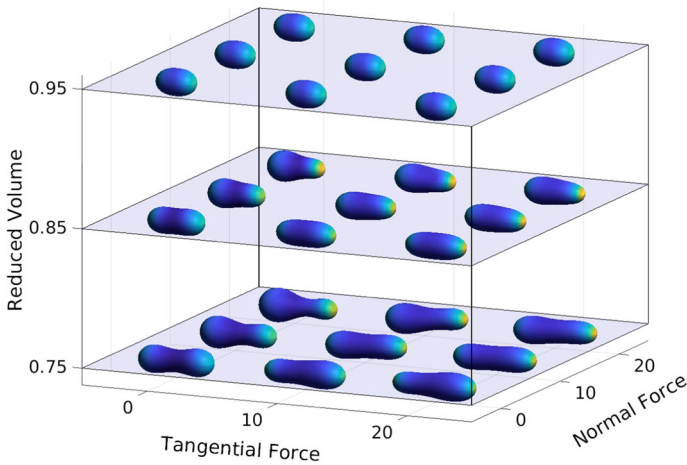


Fig. 11 The variation of cell shapes that evolve from prolate starting shapes in response to differing levels of normal and tangential forces, and at several reduced volume levels

in the pseudo-evolution Eqs. (9) and (10). The functions $f^n(u^1, u^2)$ and $f^t(u^1, u^2)$ are scalar valued functions of the surface coordinates that gives the force magnitude in the normal/tangential directions at each point on the surface, and though these forces are considered in non-dimensional form, the force magnitude is on the order of $0.1 pN/\mu m^2 - 10 pN/\mu m^2$ in dimensional terms.

6.1 Uniform moduli

We now discuss a phase-diagram showing how the cell shapes are altered at various levels of reduced volume, under different combinations of normal and tangential forces. This diagram is shown in Fig. 11 for prolate shapes, and Fig. 12 for oblate starting shapes. We set the forces in Eqs. (39) and (40) to increase linearly from zero from left to right along the x -axis, which we have chosen to align with the radial symmetry of the starting shapes. In order to avoid a discontinuity at the right-hand pole of a cell when tangential forces are imposed, we modify $f^t(u^1, u^2)$ in a small region near the pole by multiplying it by a smooth function of the x -axis coordinate that is zero at the pole and increases rapidly to one away from the pole.

Note that in each case the effects of the normal and tangential forces are in opposition to some degree. For instance, in the prolate phase-diagram, one can see that at each reduced volume level, combinations of normal and tangential forces lead to less deformed shapes than normal or tangential forces alone. This is more difficult to observe in the oblate diagram, as there is greater variation in the shapes that occur. At low force levels the steady state shapes tend to be discocytes (cup-like), but at high levels of tangential forces the oblate shapes transform into more prolate steady-states. However, a significant effect can be seen for shapes with large δf^t as δf^n is increased from 0. At zero normal force the prolate shape has the larger bulb at the right end, but it switches to the left as the normal force is increased. We also note that there are

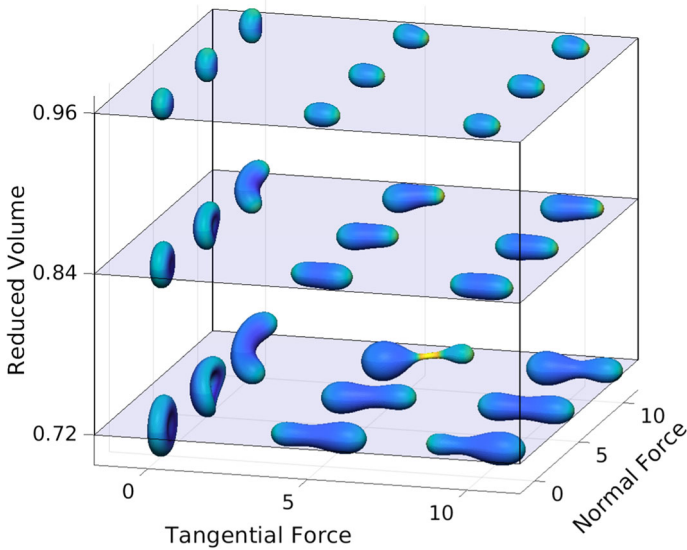


Fig. 12 Variation of initially-oblate cells in response to different levels of normal and tangential forces at several reduced volume levels. In many cases the oblate shapes are transformed into prolate shapes under the applied forces

interesting shapes obtained as the equilibria are approached. For instance, in Fig. 13, various non-axisymmetric shapes are obtained as the oblate starting shape eventually reaches a prolate equilibrium shape under application of forces. Furthermore, note that without forces, there is some degree of bistability since for given reduced volumes, there can be multiple local minima of the Helfrich energy, but in some cases, this bistability appears to vanish under strong enough forces. In particular, it seems as though large enough tangential forces applied to oblate shapes can lead to a transition towards prolate shapes (e.g. notice the similarity between the results with $\delta f^n = 0$ and $\delta f^t = 10$ in Figs. 11 and 12).

6.2 Shape changes with heterogeneous bending moduli

While a number of studies have analyzed the oblate, prolate, and stomatocyte minimizers of the Helfrich energy, few have considered the effect of variations in the bending or Gaussian-curvature moduli. In living cells, the cortical layer underlying the cell membrane varies in thickness, and due to the tight coupling between the two layers, the thickness of the cortical layer may well lead to variations in the bending moduli between different regions of the cell. This is especially relevant since to first order the bending rigidity k_B is expected to scale as h^α with the thickness h , where $\alpha \approx 2$ for a bilayer membrane (Bermudez et al. 2004) and $\alpha = 3$ for a rigid plate (Boal 2002). Since the force will also scale with h , this suggests the potential for complex mechanical control mechanisms where cells affect shape changes through a

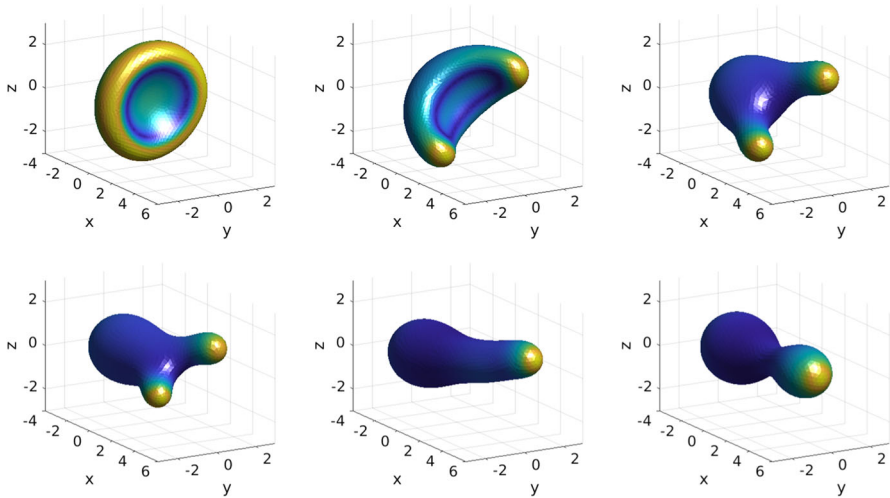


Fig. 13 Sequence of intermediate shapes as cell transforms from oblate starting shape to a prolate equilibrium after forces are added. In this case, $\delta f^n = \delta f^t = 10$. Note that the final shape shown here is not quite at steady state and so does not look exactly like the equilibrium shape in Fig. 12 at $\delta f^n = \delta f^t = 10$

combination of cortical forces and regulation of the passive mechanical properties of the membrane-cortex system.

To understand the effects of variations in the moduli, we defined various forms of variation in the moduli and then computed the stationary shapes. In particular, consider a cylindrical coordinate frame such that any point $(x, y, z) \in \mathbb{R}^3$ is written as $(x, r \cos \theta, r \sin \theta)$. If the cell is radially symmetric, then we could describe the cell shape by a function $r = r(x)$ independent of θ .

Now, let $d_x = \max x - \min x$ be the length of the cell along its axis of radial symmetry. Then we impose a variation in the modulus as

$$k_B(x) = 1 + \frac{\delta k_B}{2} \left(1 + \tanh \left(2\pi \frac{x - \bar{x}}{d_x} \right) \right) \tag{41}$$

where \bar{x} is the midpoint of the cell, and δk_B a parameter used to adjust the magnitude of the variation in the modulus. The same variation is applied to the Gaussian curvature modulus as well with δk_B replaced by δk_G . In Fig. 14 we show how the prolate branch shapes are altered in the presence of variations in the bending modulus and Gaussian-curvature modulus for several values of δk_B and δk_G . As expected, significant variations in the cell shape occur when the moduli vary across the surface, and the effects of δk_B and δk_G are different. In areas where the bending modulus k_B is large (the left bulb of the cells in 14), the bending energy is reduced by deformations that increase the radius of curvature of the surface (and hence reduce H) in the high- k_B regions. The net effect is that the left-hand bulb of the cells grows and the right bulb shrinks. On the other hand, large k_G areas tend to become saddle shaped, but the overall effect on the entire surface is more difficult to understand. In some cases, the saddle-like region between the two bulbs of the prolate cells can become

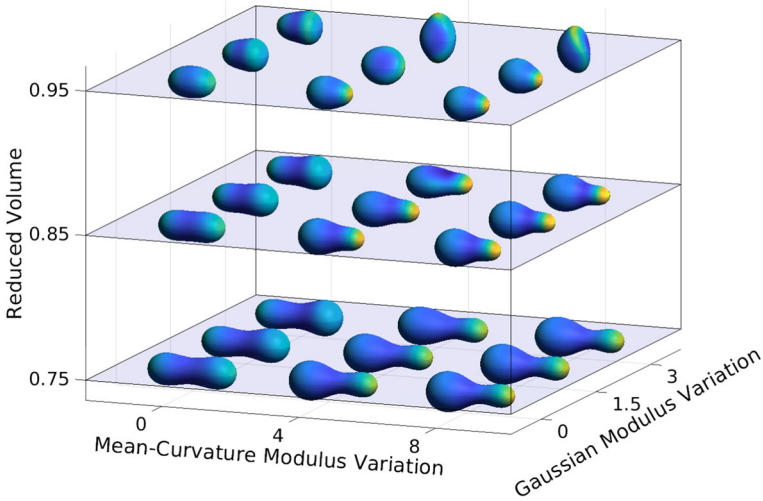


Fig. 14 A phase diagram depicting some of the different CH energy minimizers that occur in the presence of variations in the bending moduli in the absence of applied forces. Mean-curvature modulus variations refer to changes in k_B and Gaussian modulus variations refer to changes in k_G . To aid visualization, the cells have been oriented such that k_B and k_G are increasing from right to left in this figure, with maxima at the left pole of the cells

accentuated and eventually lead to a loss of axisymmetry. In other cases, axisymmetry is maintained, but the rightward-bulb of the cell becomes enlarged relative to the left. However, more work is needed to understand exactly how the various forces are balancing to induce these changes.

The above effects are seen for small to moderate axisymmetric variations. Larger deviations unfortunately cause difficulty for the numerical methods, and so were not explored here. However, later on we do explore some effects of non-axisymmetric variations, and it appears that quite different behaviors can be observed in that setting.

Interestingly, some of the shapes obtained by varying δk_B and δk_G closely resemble shapes obtained under normal and/or tangential forces. In Fig. 15, we compare the shape with $\delta k_B = 8$ to that for $\delta f^n = 15$.

In Fig. 14, the shapes are axisymmetric, which may be expected since the variation in k_B and k_G preserve axisymmetry, but in some cases this symmetry is lost. This can be understood by looking at the energetics. In Fig. 16, we plot the distribution of k_B over the surface. One can see that the final equilibrium shape has flatter regions (lower H) where k_B is high, separated by more sharply curved regions of low k_B .

However, in living cells, it may be that more complex variations in the bending moduli can be induced. For instance, if the cell is to achieve more intricate changes in shape, there must be mechanisms by which symmetries such as radial symmetry can be broken. While a full discussion of how cells may implement such mechanisms is beyond the scope of our work here, we present a few example shapes that result from non-axisymmetric moduli variations in Fig. 17. There we have set

$$k_B(\mathbf{x}) = 1 + \frac{\delta k_B}{2} \left(1 + \tanh \left(2\pi \frac{x - \bar{x}}{d_x} \right) \right) e^{-5(y/d_r)^2} \tag{42}$$

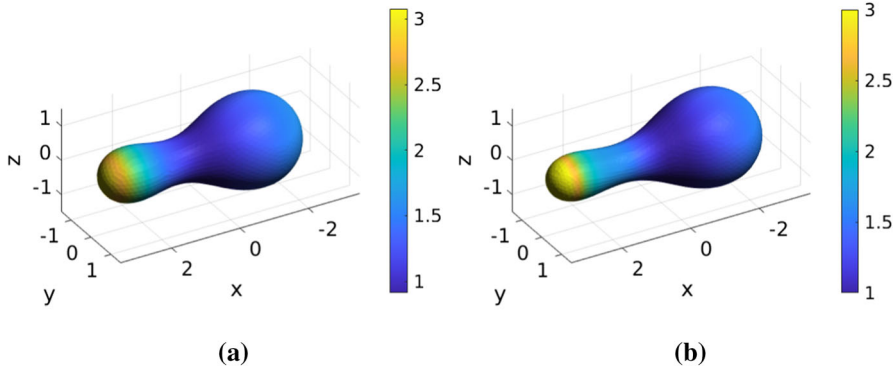
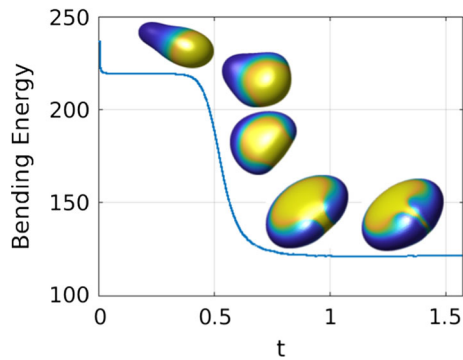


Fig. 15 In **a** the equilibrium shape for $\delta k_B = 8$ is shown, and in **b** the equilibrium shape for $\delta f^n = 15$ is shown. The resulting shapes are quite similar in appearance. The reduced volume is 0.75 in these images

Fig. 16 Evolution of the distribution of k_B over the surface as it deforms. Coloring corresponds to k_B which ranges from 1 (dark blue) to 6 (yellow). The y -axis is the bending energy, computed as an integral over the surface from Eq. (2). The first shape is axisymmetric, and one can see that as the axisymmetry is broken, there is a significant drop in the bending energy



where d_x is as above, and d_r is the maximum radius of the cell in the (y, z) -plane (and likewise for k_G). The resulting modulus variation yields a thin strip of membrane with an elevated modulus varying from front to back. Some resulting equilibrium shapes are depicted in Fig. 17.

Interestingly, these non-axisymmetric bending moduli distributions have strong effects on the cell shapes. As noted earlier, for variable k_B the shell becomes flatter where k_B is large, because the membrane becomes more rigid there and this leads to less bending. One could also imagine that cells may induce such changes in bending rigidity as a means of stabilizing themselves against mechanical forces.

In contrast, non-axisymmetric variations in k_G cause a rather different set of deformations. In this case, the cell adopts a quasi-triangular appearance, with two distinct pseudopodia-like regions. The fact that such a shape is obtained can be explained in terms of the variation in k_G since the region between the two pseudopodia exhibits a saddle-structure where the Gaussian modulus is negative (see Fig. 17 bottom row), and since k_G is largest in that region, this facilitates minimization of the Gaussian curvature energy term. While other mechanisms describing cytoskeletal force generation have been proposed for the formation of such appendages in cells, it would be

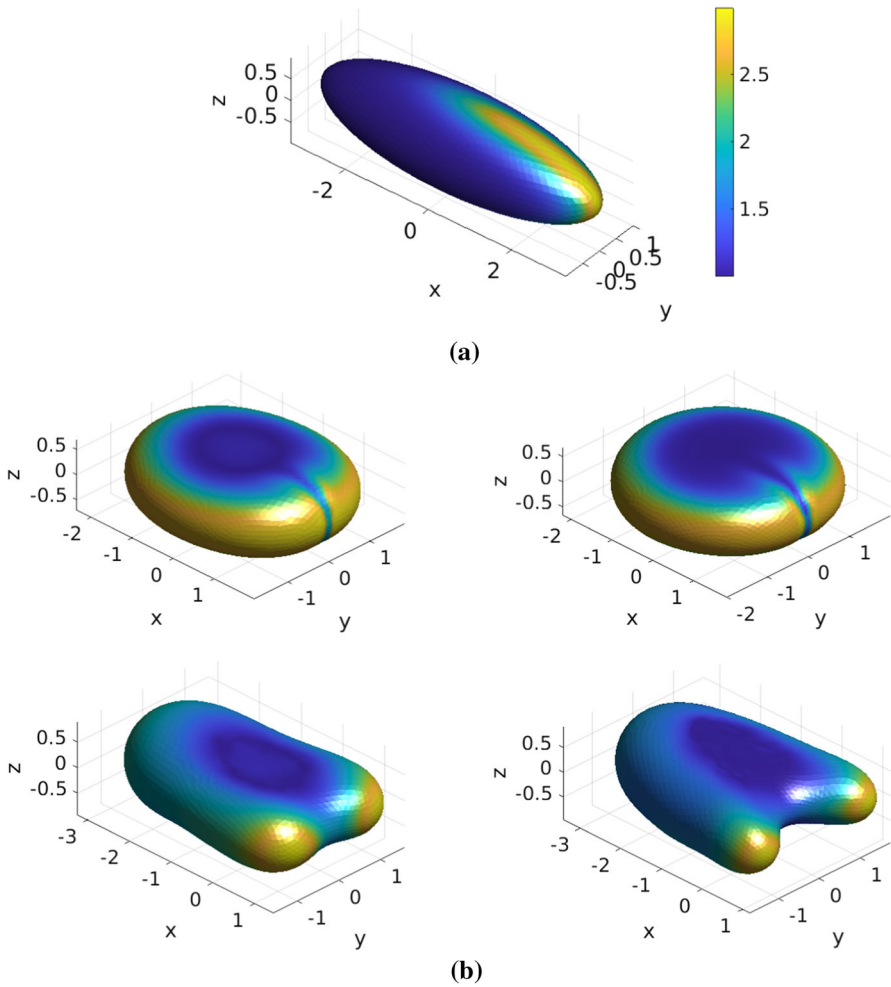


Fig. 17 **a** Starting shape with coloration corresponding to the initial bending modulus distribution. **b** Steady-state shapes for non-axisymmetric variations in the bending moduli. In the top row, k_B is varied, and in the bottom row, k_G is varied. The coloration corresponds to the curvature in **(b)**. The left images in **(b)** are for $\delta k_{B,G} = 2$ and the right images are for $\delta k_{B,G} = 4$

interesting to determine if cells have a means of adjusting k_G to facilitate such shape deformations.

When one compares these results with the effect of δk_B and δk_G for axisymmetric initial shapes, it appears that radial symmetry imposes some degree of stability in the shape of the cell, and once broken, a cell may undergo more significant deformations that would have otherwise been impossible. This is not surprising since radial symmetry can essentially be thought of as a constraint on the cell motion, and without radial symmetry larger deformations may be possible for a given amount of energy input.

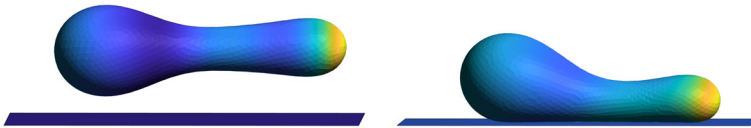


Fig. 18 A cell that is axisymmetric when free-floating encounters an adhesive membrane, leading to a loss of symmetry as the cell adheres to the membrane. Left is pre-adhesion, right is post-adhesion. The left-right asymmetry is due to a normal forces being applied in a linearly increasing density from left to right

7 The shape of cells in contact with a surface

We next consider the interaction of a cell with a rigid surface. This has been considered in the axisymmetric case in Raval and Gozdz (2020), and here we suppose that the symmetry is broken. This occurs when an initially-axisymmetric cell—here with a prolate shape—interacts with a planar surface (see Fig. 18).

Such situations are common in biology where cells can adhere to various extracellular structures. In particular, cells can use finely controlled adhesion to induce motion by modulating intracellular forces in response to the local extracellular forces.

Here we consider a planar surface that interacts via adhesion with the cell membrane. We will denote the cell membrane as \mathcal{S} (as before), and the planar surface as \mathcal{P} . As a general starting point, we assume that this adhesive-interaction arises from some sort of interaction energy, and that this adhesion energy depends upon the proximity of the cell-membrane to the surface. In particular, we assume that \mathcal{S} is smooth enough that for each $\mathbf{x} = (x_1, x_2, x_3) \in \mathcal{S}$, we can consider a small square neighborhood of area dA centered at \mathbf{x} inscribed onto \mathcal{S} . Since \mathcal{P} is planar, the same can be done at each $\mathbf{y} = (y_1, y_2, y_3) \in \mathcal{P}$. Then, we assume that the adhesion energy acting on these two subsurfaces is of the form

$$\mathcal{E}_{\text{adh}}(dA_{\mathbf{x}}, dA_{\mathbf{y}}) = U(\mathbf{x}, \mathbf{y})dA_{\mathbf{x}}dA_{\mathbf{y}}$$

This assumes the existence of some function $U(\cdot, \cdot)$ that has units of energy/(length)⁴ that characterizes pairwise interactions between points on \mathcal{S} and \mathcal{P} . When the interaction takes this form, the total adhesion energy acting on $dA_{\mathbf{x}}$ is found by summing over all disjoint $dA_{\mathbf{y}}$. In the limit $dA \rightarrow 0$, this results in

$$e_{\text{adh}}(dA_{\mathbf{x}}, \mathcal{P}) \equiv \frac{\mathcal{E}_{\text{adh}}(dA_{\mathbf{x}}, \mathcal{P})}{dA_{\mathbf{x}}} = \int_{\mathcal{P}} U(\mathbf{x}, \mathbf{y})d\mathbf{y}$$

where the left-hand side represents an energy density with respect to area on \mathcal{S} . Since the area of dA is independent of \mathbf{x} , we can just write this as $e_{\text{adh}}(\mathbf{x}, \mathcal{P})$. The force on \mathbf{x} is then found as $\mathbf{F}_{\text{adh}}(\mathbf{x}) = -\nabla_{\mathbf{x}}e_{\text{adh}}(\mathbf{x}, \mathcal{P})$. All that remains now is to specify $U(\mathbf{x}, \mathbf{y})$. For simplicity, we suppose that this takes the form of a Lennard–Jones potential, and set

$$U(\mathbf{x}, \mathbf{y}) = 4k \left(\left(\frac{\sigma}{\|\mathbf{x} - \mathbf{y}\|} \right)^{12} - \left(\frac{\sigma}{\|\mathbf{x} - \mathbf{y}\|} \right)^6 \right)$$

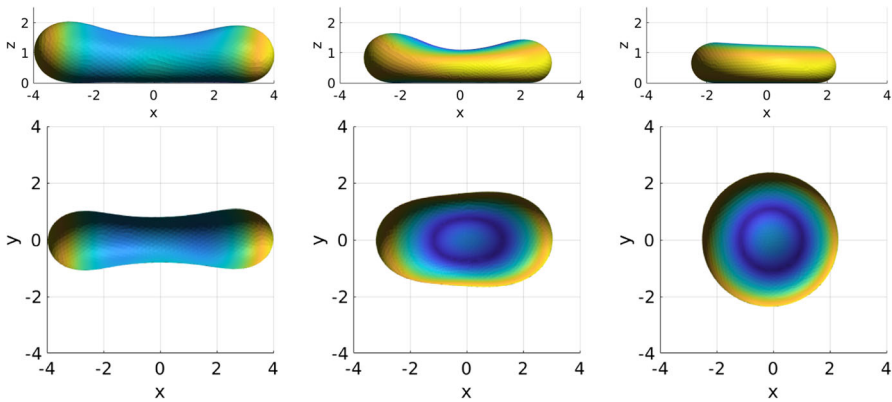


Fig. 19 Depiction of cells that are adhered to a surface at $z = 0$. There is a left-to-right asymmetry due to a linearly increasing adhesivity ($k(x)$ in Eq. (43)), with stronger adhesion at the right-hand side of the cell. At low levels of adhesion (left-hand figures, $\max k = 1$), the cell retains a prolate shape, whereas under strong adhesion (right-hand figures, $\max k = 3$) the resting state becomes flattened out. In the top row, the view is looking at the profile of the cell with $z = 0$ on the bottom. The bottom row is an overhead view of the adhered cells. Notice that under low adhesion, the cell retains a prolate shape, whereas as the adhesion increases, a more oblate shape is obtained. On the right, the shape is nearly axisymmetric because the adhesion level is quite strong uniformly, even though there is still a gradient from left-to-right

where σ is a characteristic length of the interaction, and for dimensional consistency, we must have that k is an energy/(length)⁴. Since this choice of $U(x, y)$ depends only on $\|\mathbf{x} - \mathbf{y}\|$, we can write $U(R) \equiv U(x, y)$ for shorthand where $R = \|\mathbf{x} - \mathbf{y}\|$. Given our assumption that \mathcal{P} is a planar surface of infinite extent, we can compute $\mathbf{F}_{\text{adh}}(\mathbf{x}, \mathcal{P})$ explicitly as

$$\begin{aligned} \mathbf{F}_{\text{adh}}(\mathbf{x}, \mathcal{P}) &= -\nabla_{x_1, x_2, x_3} \left[\int_0^{2\pi} \int_0^\infty U\left(\sqrt{r^2 + x_3^2}\right) r dr d\theta \right] \\ &= 8\pi z k \left(\left(\frac{\sigma}{z}\right)^{12} - \left(\frac{\sigma}{z}\right)^6 \right) \mathbf{e}_z = 2\pi z U(z) \mathbf{e}_z \end{aligned} \tag{43}$$

where $x_3 = z$ is the distance (height) of the membrane point from the boundary.

While this last result depended on a specific choice for the pairwise interaction, other types of interaction potentials can just as well be substituted. For instance DLVO-theory and polymer brush models are often used to describe adhesion in biological settings (Israelachvili 2011). We do not expect that these different interaction potentials will qualitatively change the resulting cell shapes up to a choice of parameters that govern how strong the attractive/repulsive forces are.

Finally, since cells can modulate their adhesive interactions with the environment, we expect that k and σ could potentially vary along the cell membrane. Thus, we also consider the case with the adhesion parameter, k increasing from front-to-back (left-to-right in Figs. 18 and 19) along the length of a cell.

The resulting shapes that occur with various levels of adhesion strength in the membrane are shown Fig. 19.

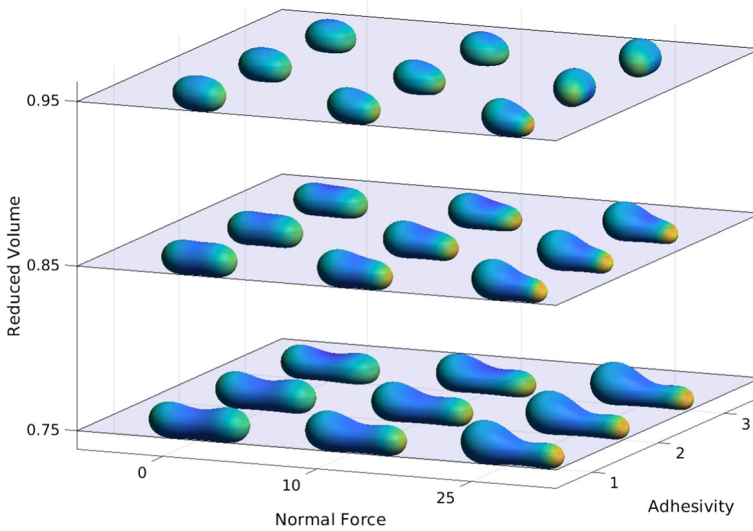


Fig. 20 Effect of forces, reduced volume, and adhesion on cell shape. It is noteworthy that the roundedness, which increases as adhesivity is decreased and the reduced volume is increased, resembles the mesenchymal-to-amoeboid transition that plays an important role in the transition from stationary cells to migratory cells in cancer metastasis and other contexts

In Fig. 19, we see how the shape of cells is altered with adhesion to a surface. Interestingly, the results appear quite different than those found in Raval and Gozdz (2020) (depicted in Fig. 4). This discrepancy likely arises from several differences in our simulations, and possibly due to the presence of multiple minimizers of the Helfrich energy.

In Fig. 20 we show a phase diagram with various shapes obtained under several levels of adhesion, normal forces, and reduced volumes.

As the reduced volume is lowered, we observe that the adhered cells are able to increase their contact area with the surface leading to flatter shapes, whereas for higher reduced volume, the cells remain fairly spherical. Since cell volume (and hence sphericity) is controlled over longer timescales in part by osmotic pressure balances and transport of fluid through the cell membrane, this suggests the potential for interesting interactions between cell adhesion and osmotic control. As an example, in glioblastoma tumor cells, it has been theorized that cells are able to migrate through brain tissue by clinging to blood vessels and modulating their fluid content to slip past obstacles (Cuddapah et al. 2014).

8 Discussion

The current work serves to better understand how cortical forces determine cell shapes, and this can be used to determine the modes of blebbing and how the internal and external fluids affect the cell motility. To this end we herein proposed a high-level description of the membrane-cortex interaction that incorporates both the elasticity

of the combined cell membrane and cortex that can be used to study the role of intra- and extracellular fluids. Our aim here was to first identify general principles – for example, how does tension affect cell morphology and the intercellular pressure – before developing more detailed models. As a result, what is learned will be broadly applicable to many cell types.

A number of interesting results are already attainable at this level of modeling. For instance, it appears that active force generation, as well as modulation of passive mechanical properties such as bending rigidities may play important roles in coordinating complex motion that cells undertake as they explore their local environment or undergo directed motion.

While many studies have considered the crucial role that the cytoskeleton plays in directing cell movement, we have also seen that reduced volume has a very strong effect on cell shape. This suggests that osmotic pressure variation, and subsequent mass transport across a cell membrane may play an important role in conjunction with cytoskeletal mechanics in determining the movement patterns of a cell.

In the context of a cell adhering to a surface, the contact region between the cell and the surface depends upon the reduced volume of the cell, and a cell that can control its reduced volume level via mass transport across its membrane, may be able to additionally adjust its adhesion to a surface.

An interesting and important adaptability between two leading modes of motion – tension-driven cell swimming and cyclic-blebbing cell swimming – is implied by our work. In a highly confined environment, such as a narrow microfluidic channel, the abilities of extension and propagation of cyclic small blebs of the blebb-driven cells is suppressed. While a natural way to overcome this for an efficient locomotion is that the cells adopt a retrograde cortical flow, which provides the tangential forces on the cell surface (Wu et al. 2018), to propel themselves.

To further understand how cells are able to coordinate these distinct aspects of shape control in order to achieve efficient and effective motion in response to external or internal signals will require a great deal of theoretical and experimental work, and there are many future directions that may be of interest.

Acknowledgements This work was supported in part by NSF Grant DMS 1311974, and NIH Grant 54-CA-210190, the Newton Institute and the Simons Foundation. We thank a reviewer for a very thorough reading of the work that brought a number of minor errors to our attention.

Appendix A Summary of surface notation

Notation and basic quantities

A smooth surface $S \subset \mathbb{R}^3$ will be parameterized by $u = (u^1, u^2)$ and the position vector in \mathbb{R}^3 to the surface is denoted $\mathbf{x}(u)$. The surface tangent vectors (which may be nonunitary) at each point on S are defined by the parametric derivative of \mathbf{x} with respect to the surface coordinates, namely,

$$\mathbf{e}_i(u^1, u^2) = \frac{\partial \mathbf{x}}{\partial u^i}(u^1, u^2) \quad i = 1, 2 \quad (\text{A1})$$

and the surface normal \mathbf{n} is defined by the relations $\mathbf{n} \cdot \mathbf{e}_i = 0$, $\mathbf{n} \cdot \mathbf{n} \equiv \langle \mathbf{n}, \mathbf{n} \rangle = 1$. The covariant metric tensor of the surface is defined as $g_{ij} = \mathbf{e}_i \cdot \mathbf{e}_j$, the contravariant surface metric tensor is the inverse tensor defined by the relation $g_{ij}g^{jk} = \delta_i^k$, and the determinant of g_{ij} is denoted by $g \equiv \det(g_{ij})$. The contravariant basis vectors, denoted \mathbf{e}^i are the dual basis vectors to the covariant basis vectors, and are defined via $\mathbf{e}^i = g^{ij}\mathbf{e}_j$. Here and hereafter a repeated upper and lower index denotes summation.

The Levi-Civita symbol is defined in covariant and contravariant form as

$$\begin{aligned} \epsilon_{ij} &= e_{ij}\sqrt{g} \\ \epsilon^{ij} &= e_{ij}/\sqrt{g} \end{aligned}$$

where $e_{12} = -e_{21} = 1$ and $e_{11} = e_{22} = 0$.

The second derivative of \mathbf{x} is given by Gauss' formula

$$\mathbf{e}_{i,j} \equiv \frac{\partial^2 \mathbf{x}}{\partial u^i \partial u^j} = \Gamma_{ij}^k \mathbf{e}_k + B_{ij} \mathbf{n}, \tag{A2}$$

where \mathbf{n} is the outward normal to the surface and the factor Γ_{ij}^k is called a Christoffel symbol and is defined as

$$\Gamma_{ij}^k = \mathbf{e}^k \cdot \frac{\partial \mathbf{e}_i}{\partial u^j}. \tag{A3}$$

This is a surface directional derivative in the direction of \mathbf{e}_i , where \cdot, i denotes the derivative with respect to u^i . The components of the surface curvature tensor B are defined as

$$B_{ij} = \mathbf{n} \cdot \mathbf{e}_{i,j} = -\mathbf{n}_{,j} \cdot \mathbf{e}_i. \tag{A4}$$

Weingarten's equation relates the variation of the normal to the curvature tensor via

$$\mathbf{n}_{,i} = -B_i^j \mathbf{e}_j, \tag{A5}$$

where $B_i^j = g^{ik} B_{kj}$ is found by raising the first index of B_{ij} . The mean curvature is $H = -\frac{1}{2}B_i^i$, and the Gaussian curvature is given by $K = \det(B_i^j)$.

Derivatives in the direction of the tangent vectors or their dual are called covariant derivatives. The components of the covariant derivative of a co- and contravariant vector \mathbf{w} defined on \mathcal{S} are

$$\nabla_j(w_i) \equiv \frac{\partial w_i}{\partial u^j} - w_k \Gamma_{ij}^k \quad \text{and} \quad \nabla_j(w^i) \equiv \frac{\partial w^i}{\partial u^j} + w^k \Gamma_{kj}^i, \tag{A6}$$

where in each case the second term accounts for the variation of the basis on the surface. This leads to definitions of the gradient and divergence of a vectorfield on \mathcal{S} as follows.

Hereafter we consider only contravariant vectors and define $\nabla_s(\cdot) \equiv \nabla_i(\cdot)e^i$; then the surface gradient of a scalar is the standard parametric gradient

$$\nabla_s F = (\nabla_i F)e^i \tag{A7}$$

and the surface gradient of a contravariant vector is

$$\begin{aligned} \nabla_s \mathbf{F} &= e^i \nabla_i (F^j e_j + F^n \mathbf{n}) \\ &= e^i F^j_{;i} e_j + e^i F^n_{;i} \mathbf{n} + e^i F^n n_{;i} \\ &= \left(F^j_{;i} - F^n B^j_i \right) e^i e_j + \left(F^j B_{ji} + F^n_{;i} \right) e^i \mathbf{n}. \end{aligned} \tag{A8}$$

where a semicolon denotes the covariant derivative, *i.e.*, $\nabla_i w^j \equiv w^j_{;i}$.

The divergence of a vectorfield is given by

$$\nabla_s \cdot \mathbf{F} = \nabla_i (F^j e_j + F^n \mathbf{n}) \cdot e^i = F^j_{;j} - F^n B^i_i = F^j_{;j} + 2HF^n$$

In particular we have

$$\nabla_s \cdot \mathbf{n} = e^i \nabla_i \cdot \mathbf{n} = -B^j_i e^i \cdot e_j = -B^i_i = 2H. \tag{A9}$$

Finally, we have the following definitions for the Laplacian, and a modified Laplacian that appear in the pseudo-evolution equations when k_G is variable,

$$\Delta_s f = \frac{1}{\sqrt{g}} \partial_i \left(\sqrt{g} g^{ij} \partial_j f \right), \quad \overline{\Delta}_s f = \frac{1}{\sqrt{g}} \partial_i \left(\sqrt{g} K B^{ij} \partial_j f \right),$$

where f is an arbitrary smooth function.

Appendix B Hodge decomposition of vector fields on 2-Manifolds

For any smooth vector field in \mathbb{R}^3 , the Hodge-Helmholtz decomposition states that this vector can be written as the sum of several components in the following way,

$$\mathbf{v} = \mathbf{v}_s + \mathbf{v}_c + \mathbf{h} \tag{B10}$$

where \mathbf{v}_s is irrotational, \mathbf{v}_c is divergence free, and \mathbf{h} is a harmonic function. In fact, these three components are unique, and mutually orthogonal. This follows from the identities $\nabla \cdot \nabla \times \mathbf{a} = 0$, and $\nabla \times \nabla b = 0$ for vector field \mathbf{a} and scalar field b . This allows us to write the decomposition explicitly as

$$\mathbf{v} = \nabla \phi + \nabla \times \boldsymbol{\psi} + \mathbf{h}. \tag{B11}$$

where ϕ is a scalar field and $\boldsymbol{\psi}$ is a vector field. Unfortunately, there is no analogous curl operator when the dimension of the space is not 3.

However, with some modifications, this decomposition generalizes to manifolds with arbitrary dimension so long as the differential operators corresponding to the gradient, divergence, and curl are appropriately redefined. The general case is known as the Hodge-decomposition which is a standard topic in differential geometry texts (Renteln 2013). Rather than introducing the significant amount of new notation required to define the Hodge-decomposition, we will apply the main results to 2-dimensional manifolds embedded in \mathbb{R}^3 .

In the language of differential geometry, smooth functions on a manifold, \mathcal{M} are called 0-forms, and “vectors” defined contravariantly as

$$\alpha = \alpha_i e^i \tag{B12}$$

are known as 1-forms. In a 2-dimensional manifold, there are also 2-forms which are defined as linear combinations of anti-symmetrized tensor products of two 1-forms, or

$$\gamma = \frac{1}{2}(\alpha_i \beta_j - \alpha_j \beta_i) e^i e^j = \alpha \wedge \beta. \tag{B13}$$

In the 2-dimensional setting, the dimension of the space of 2-forms is one, hence we can label $\mathbf{J} = e^1 \wedge e^2 = e^1 e^2 - e^2 e^1$ as the single linearly independent 2-form, and write

$$\alpha \wedge \beta = \frac{1}{2}(\epsilon^{ij} \alpha_i \beta_j) \mathbf{J} \tag{B14}$$

where ϵ^{ij} is the 2-dimensional Levi-Civita symbol. With this in mind, the Hodge-decomposition theorem states that for any 1-form \mathbf{v} , we may write

$$\mathbf{v} = \nabla_i \phi e^i + \epsilon^{ij} \nabla_i \psi e^j + \mathbf{h} \tag{B15}$$

where \mathbf{h} satisfies $\nabla_s \cdot \mathbf{h} = 0$ and $\nabla_s \times \mathbf{h} = 0$. In this case ϕ is a 0-form and ψ is the density of a two form, $\psi \mathbf{J}$. Furthermore, because we are assuming S is a closed-surface, $\mathbf{h} \equiv \mathbf{0}$.

If we identify $\epsilon^{ij} \nabla_i \psi$ with $(\nabla_s \times \psi)^j$ then we have recovered an analog of the Helmholtz-decomposition for a 2-dimensional closed manifold,

$$\mathbf{v} = \nabla_s \phi + \nabla_s \times \psi. \tag{B16}$$

On two-dimensional manifolds, there is a second curl operator which takes 1-forms to 2-forms. It is defined by

$$\nabla_s \times \xi = (\epsilon^{ab} \nabla_a \xi_b) e^1 \wedge e^2. \tag{B17}$$

These two curl operators can be understood as specializations of the 3D curl operator if we consider the case of a planar surface lying in the plane $z = 0$. Let us consider a normally oriented vector field on that surface. Then the vector field can be written as

$\mathbf{v} = v^z(x, y)\mathbf{e}_z$ since the normal vector to $z = 0$ is \mathbf{e}_z . Let us extend this vector field to a vector field in \mathbb{R}^3 by multiplying it by a smooth function $\phi(z)$ where $\phi(0) = 1$ and $\phi'(0) = 0$. Then, at $z = 0$, the curl of $\tilde{\mathbf{v}} = \phi(z)\mathbf{v}(x, y)$ is

$$\nabla \times \tilde{\mathbf{v}} = \begin{vmatrix} \mathbf{e}_x & \mathbf{e}_y & \mathbf{e}_z \\ \partial_x & \partial_y & \partial_z \\ 0 & 0 & \phi v^z \end{vmatrix} = (\partial_y v^z \mathbf{e}_x - \partial_x v^z \mathbf{e}_y).$$

and this is precisely what $\nabla_s \times v^z$ reduces to. Thus for a flat surface, $\nabla_s \times \psi \equiv \nabla \times (\psi \mathbf{n})$. The second curl operator can be found by considering the curl of vector fields $\mathbf{v} = v^x \mathbf{e}_x + v^y \mathbf{e}_y$. Extending to $\tilde{\mathbf{v}} = \phi(z)\mathbf{v}(x, y)$, we can compute $\nabla \times \tilde{\mathbf{v}}$ as above. This will yield that the coefficient of $\nabla_s \times \mathbf{v}$ is the coefficient of the normal component of $\nabla \times \tilde{\mathbf{v}}$.

Finally, for a two-form with density ψ ,

$$\begin{aligned} \nabla_s \times (\nabla_s \times \psi) &= \epsilon^{ab} \nabla_a (\epsilon^{bc} \nabla_c \psi) = \epsilon^{ab} \epsilon^{bc} \nabla_a \nabla_c \psi \\ &= \epsilon^{ab} \epsilon_{bc} \nabla_a \nabla^c \psi = -\Delta_s \psi \end{aligned}$$

These identities allow us to recover ϕ and ψ given \mathbf{v} as

$$\begin{aligned} \nabla_s \cdot \mathbf{v} &= \Delta_s \phi \\ \nabla_s \times \mathbf{v} &= -\Delta_s \psi \end{aligned}$$

and see that this decomposition is orthogonal in the sense that

$$\int_S (\nabla_s \phi) \cdot (\nabla_s \times \psi) dS = - \int_S \phi \nabla_s \cdot (\nabla_s \times \psi) dS = 0. \tag{B18}$$

Appendix C Derivation of weak curvature forces

We sketch the derivation of Eq. (15). The derivation of these equations with $k_B = 1$ and $C_0 = 0$ is presented in detail in Dziuk (2008).

First, consider the area integral,

$$A(\mathcal{S}) = \int_{\mathcal{S}} dS = \int_U \sqrt{g} dA$$

where \mathcal{S} is the membrane embedded in \mathbb{R}^3 and $U \subset \mathbb{R}^2$ is the image of a local coordinate chart on \mathcal{S} (in the case where \mathcal{S} cannot be covered by the inverse image of U , this is extended to a collection of U_i that cover \mathcal{S} so long as \mathcal{S} is smooth and bounded).

Let \mathbf{x} be the identity on S (e.g. $S = \{\mathbf{x}\}$), and consider a variation $\mathbf{x} \mapsto \mathbf{x} + \epsilon \delta \mathbf{x}$ with $S_\epsilon = \{\mathbf{x} + \epsilon \delta \mathbf{x}\}$. Then the variational derivative with respect to ϵ of A ,

$$\lim_{\epsilon \rightarrow 0} \frac{A(S_\epsilon) - A(S_0)}{\epsilon} \equiv \delta A(\delta \mathbf{x})$$

is found as

$$\delta A(\delta \mathbf{x}) = \int_U \delta \sqrt{g} \delta \mathbf{x} dA = \int_U \sqrt{g} (\nabla_s \cdot \delta \mathbf{x}) dA = \int_S \nabla_s \cdot \delta \mathbf{x} dS = \int_S \nabla_s \mathbf{x} : \nabla_s \delta \mathbf{x} dS$$

where the last step is possible since, in terms of contravariant derivatives,

$$\nabla_s \cdot \delta \mathbf{x} = \nabla_i \delta x^i = \mathbf{e}^i : \nabla_k (\delta \mathbf{x}) \mathbf{e}^k = \nabla_s \mathbf{x} : \nabla_s \delta \mathbf{x}$$

But, with sufficient regularity of S ,

$$\int_S \nabla_s \mathbf{x} : \nabla_s \delta \mathbf{x} dS = - \int_S \Delta_s \mathbf{x} \cdot \delta \mathbf{x} dS = \int \mathbf{H} \cdot \delta \mathbf{x} dS$$

Thus, if we consider the integral

$$E(S) = \int_S k_B |\mathbf{H} + C_0 \mathbf{n}|^2 dS,$$

and let \mathbf{x} be varied as $\mathbf{x} \mapsto \mathbf{x} + \epsilon \delta \mathbf{x}$, then

$$\delta E(\delta \mathbf{x}) = \frac{1}{2} \int_U k_B |\mathbf{H} + C_0 \mathbf{n}|^2 \delta(\sqrt{g}) [\delta \mathbf{x}] dA + \int_U k_B \delta \mathbf{H} [\delta \mathbf{x}] \cdot (\mathbf{H} + C_0 \mathbf{n}) \sqrt{g} dA \tag{C19}$$

$$= \frac{1}{2} \int_S k_B |\mathbf{H} + C_0 \mathbf{n}|^2 (\nabla_s \cdot \delta \mathbf{x}) dS + \int_S k_B \delta \mathbf{H} [\delta \mathbf{x}] \cdot (\mathbf{H} + C_0 \mathbf{n}) dS \tag{C20}$$

where we have assumed that k_B does not change with variations in \mathbf{x} and that C_0 is a constant. We have also used the fact that $\delta \mathbf{n} \cdot \mathbf{n} = 0$ in the above formula. The term $\delta \mathbf{H}$ will be defined weakly as linear operator acting on $\delta \mathbf{x}$. Following the same steps as in Dziuk (2008), we simplify by considering the variational derivative of the relation

$$\int_S \mathbf{H} \cdot \delta \mathbf{x} dS = \int_S \nabla_s \mathbf{x} : \nabla_s \delta \mathbf{x} dS \tag{C21}$$

to obtain $\delta \mathbf{H}$ weakly. Since the variation $\delta \mathbf{x}$ already appears in Eq. (C21), this is essentially the calculation of a second-order variational derivative of $A(S)$. This leads

to a bilinear functional $\delta H(\boldsymbol{\psi}, \delta \mathbf{x})$ where $\delta \mathbf{x}$ and $\boldsymbol{\psi}$ are arbitrary smooth functions. Replacing $\boldsymbol{\psi}$ by $\mathbf{H} + C_0 \mathbf{n}$ and following the calculation in Dziuk (2008) yields

$$\begin{aligned} \langle \delta H, (\mathbf{H} + C_0 \mathbf{n}), \delta \mathbf{x} \rangle &= \int_S -\mathbf{H} \cdot (\mathbf{H} + C_0 \mathbf{n}) \nabla_s \cdot \delta \mathbf{x} - \nabla_s (\mathbf{H} + C_0 \mathbf{n}) : \nabla_s \delta \mathbf{x} \\ &\quad - (\nabla_s \cdot (\mathbf{H} + C_0 \mathbf{n})) (\nabla_s \cdot \delta \mathbf{x}) \\ &\quad + (\nabla_s \delta \mathbf{x} + (\nabla_s \delta \mathbf{x})^T) \nabla_s \mathbf{x} : \nabla_s (\mathbf{H} + C_0 \mathbf{n}) dS \end{aligned} \tag{C22}$$

If in addition, there is a variable k_B , we replace $\mathbf{H} + C_0 \mathbf{n}$ by $k_B (\mathbf{H} + C_0 \mathbf{n})$. Combining the results yields Eq. (15). If C_0 is variable on the surface, there are additional terms due to the variation of

$$\int_S C_0 \mathbf{n} dS.$$

It does not appear that the resulting terms present any particular difficulties if C_0 is smooth, but we did not consider this extension in this article.

Appendix D Work done by applied forces

While the change in energy due to the various energy-related terms is straightforward to compute, the work due to the applied forces is not.

On the one hand, if the shape is in mechanical equilibrium prior to the application of forces, we must have that after a new equilibrium is established under those forces,

$$E_{new} = E_{old} + W$$

where W is the work done by the forces (assuming no dissipation occurs). However, it is also interesting to more directly obtain a result for the work done. To do so, note that the power generation due to the forces is found as

$$P(t) = \int_{S_t} \mathbf{f} \cdot \mathbf{u} dS_t$$

where S_t is the position of the surface at time t and \mathbf{u} is the surface velocity. The total work done is then

$$W = \int_0^T P(t) dt$$

In order to write this as a force times a displacement, we must account for changes in orientation of each point on the surface as it evolves.

However, since we have applied forces of the form

$$\mathbf{f}(u^1, u^2, t) = f^i(u^1, u^2) \mathbf{e}_i(u^1, u^2, t) + f^n(u^1, u^2) \mathbf{n}(u^1, u^2, t)$$

time-dependence only occurs due to the changing coordinate frame $\{e_i, n\}$ on the surface. In this sense, $f(x)$ can be understood as a rotation and translation of a time-independent vector-field f_0 on S_0 . Let us then consider normalized basis vectors \tilde{E}_i and \tilde{e}_i on S at $t = 0$ and $t = \tau > 0$ respectively (denoted by S_0 and S_τ here). Let $R(x, t)$ be the rotation matrix that maps the basis vectors of the frame $\{\tilde{E}_i, N\}$ at $X \in S_0$ to those in $\{\tilde{e}_i, n\}$ at $x(X, t)$ on S_t .⁹

Then, we can compute the power being exerted on S_t as an integral over S_0 as

$$P(t) = \int_{S_0} f_0 \cdot R^{-1} u dS_0$$

where we have assumed incompressibility of the surface at all t , and R^{-1} is the inverse map of R .

Since f_0 is constant on the reference surface, we can compute

$$W = \int_{S_0} f_0 \cdot \left(\int_0^T R^{-1}(t) u dt \right) dS_0 \equiv \int_{S_0} f_i d^i + f^n d^n dS_0.$$

To understand this, recall the reference frame $\{\tilde{E}_i, N\}$ at $t = 0$, and note that

$$\begin{aligned} \int_0^T R^{-1} u dt &= \int_0^T (\tilde{E}_i \tilde{e}^i + N n) (u^i \tilde{e}_i + u^n n) dt \\ &= \int_0^T u^i \tilde{E}_i + u^n N dt = d^i \tilde{E}_i + d^n N \end{aligned}$$

which is essentially keeping the component values of u but changing the coordinate frame to match f_0 . This essentially computes how far each point moved parallel to f during the surface evolution and thus gives us a formula involving a force times a displacement.

While this result seems useful conceptually, in practice, the work is easier to approximate either as the sum of the changes in the other energy terms, or by approximating $P(t)$ at each time step and integrating over time.

References

- Alert R, Casademunt J, Brugués J, Sens P (2015) Model for probing membrane-cortex adhesion by micropipette aspiration and fluctuation spectroscopy. *Biophys J* 108(8):1878–1886
- Barry NP, Bretscher MS (2010) Dictyostelium amoebae and neutrophils can swim. *Proc Nat Acad Sci* 107(25):11376–11380
- Bergert M, Chandradoss SD, Desai RA, Paluch E (2012) Cell mechanics control rapid transitions between blebs and lamellipodia during migration. *Proc Nat Acad Sci* 109(36):14434–14439

⁹ If $F = \frac{\partial x}{\partial X}$ is the deformation gradient of the deformation (extended to a tubular neighborhood of S), then the polar decomposition of F allows us to write $F = RU$ where R is the rotation matrix defined above, and U is a stretch matrix that describes the change in magnitude of vectors as they are mapped from S_0 to S_t . Since the force magnitude is not changing in this case, we use R which does not change the magnitude of vectors as they are mapped.

- Bermudez H, Hammer D, Discher D (2004) Effect of bilayer thickness on membrane bending rigidity. *Langmuir* 20(3):540–543
- Boal D (2002) *Mechanics of the cell*. Cambridge University Press, Cambridge
- Bonito A, Nochetto R, Pauletti M (2010) Parametric FEM for geometric biomembranes. *J Comput Phys* 229(9):3171–3188
- Bonito A, Nochetto R, Pauletti M (2010) Geometrically consistent mesh modification. *SIAM J Numer Anal* 48(5):1877–1899
- Bonito A, Nochetto R, Pauletti M (2011) Dynamics of biomembranes: effect of the bulk fluid. *Math Model Nat Phenom* 6(5):25–43
- Bovellan M, Romeo Y, Biro M, Boden A, Chugh P, Yonis A, Vaghela M, Fritzsche M, Moulding D, Thorogate R et al (2014) Cellular control of cortical actin nucleation. *Curr Biol* 24(14):1628–1635
- Canham PB (1970) The minimum energy of bending as a possible explanation of the biconcave shape of the human red blood cell. *J Theor Biol* 26(1):61–76
- Capovilla R, Guven J, Santiago J (2003) Deformations of the geometry of lipid vesicles. *J Phys A Math Gen* 36(23):6281
- Charras GT, Paluch E (2008) Blebs lead the way: how to migrate without lamellipodia. *Nat Rev Mol Cell Biol* 9(9):730–736
- Chugh P, Clark AG, Smith MB, Cassani DA, Dierkes K, Ragab A, Roux PP, Charras G, Salbreux G, Paluch EK (2017) Actin cortex architecture regulates cell surface tension. *Nat Cell Biol* 19(6):689–697
- Cortez R (2001) The method of regularized stokeslets. *SIAM J Sci Comput* 23(4):1204–1225
- Cuddapah VA, Robel S, Watkins S, Sontheimer H (2014) A neurocentric perspective on glioma invasion. *Nat Revs Neurosci* 15(7):455–465
- Dai J, Sheetz MP (1999) Membrane tether formation from blebbing cells. *Biophys J* 77(6):3363–3370
- Diz-Muñoz A, Thurley K, Chintamen S, Altschuler SJ, Wu LF, Fletcher DA, Weiner OD (2016) Membrane tension acts through PLD2 and mTORC2 to limit actin network assembly during neutrophil migration. *PLoS Biol* 14(6):1002474
- Doi M (2011) Onsager’s variational principle in soft matter. *J Phys Condens Matter* 23(28):284118
- Dziuk G (2008) Computational parametric Willmore flow. *Numer Math* 111(1):55–80
- Dziuk G, Elliott C (2013) Finite element methods for surface PDEs. *Acta Numer* 22:289–396
- Engwirda D (2016) Conforming restricted Delaunay mesh generation for piecewise smooth complexes. *Procedia Eng* 163:84–96
- Fritzsche M, Erlenkämper C, Moeendarbary E, Charras G, Kruse K (2016) Actin kinetics shapes cortical network structure and mechanics. *Sci Adv* 2(4):1501337
- Guckenberger A, Gekle S (2017) Theory and algorithms to compute Helfrich bending forces: a review. *J Phys Condens Matter* 29(20):203001
- Hawkins RJ, Poincloux R, Bénichou O, Piel M, Chavrier P, Voituriez R (2011) Spontaneous contractility-mediated cortical flow generates cell migration in three-dimensional environments. *Biophys J* 101(5):1041–1045
- Helfrich W (1973) Elastic properties of lipid bilayers: theory and possible experiments. *Zeitschrift für Naturforschung C* 28(11–12):693–703
- Hochmuth R (2000) Micropipette aspiration of living cells. *J Biomech* 33(1):15–22
- Hochmuth R, Shao J, Dai J, Sheetz M (1996) Deformation and flow of membrane into tethers extracted from neuronal growth cones. *Biophys J* 70:358–369
- Israelachvili J (2011) *Intermolecular and surface forces*. Academic press, Massachusetts
- Kapustina M, Elston TC, Jacobson K (2013) Compression and dilation of the membrane-cortex layer generates rapid changes in cell shape. *J Cell Biol* 200(1):95–108
- Keren K, Pincus Z, Allen GM, Barnhart EL, Marriot G, Mogilner A, Theriot JA (2008) Mechanism of shape determination in motile cells. *Nature* 453:475–481
- Lämmermann T, Bader BL, Monkley SJ, Worbs T, Wedlich-Söldner R, Hirsch K, Keller M, Förster R, Critchley DR, Fässler R et al (2008) Rapid leukocyte migration by integrin-independent flowing and squeezing. *Nature* 453(7191):51–55
- Lieber AD, Schweitzer Y, Kozlov MM, Keren K (2015) Front-to-rear membrane tension gradient in rapidly moving cells. *Biophys J* 108(7):1599–1603
- Liu Y-J, Berre ML, Lautenschlager F, Maiuri P, Callan-Jones A, Heuzé M, Takaki T, Voituriez R, Piel M (2015) Confinement and low adhesion induce fast amoeboid migration of slow mesenchymal cells. *Cell* 160(4):659–672
- McMahon HT, Boucrot E (2015) Membrane curvature at a glance. *J Cell Sci* 128(6):1065–1070

- Mesarec L, Gózdź W, Iglič A, Kralj-Iglič V, Virga EG, Kralj S (2019) Normal red blood cells' shape stabilized by membrane's in-plane ordering. *Sci Rep* 9(1):1–11
- Mesarec L, Drab M, Penič S, Kralj-Iglič V, Iglič A (2021) On the role of curved membrane nanodomains and passive and active skeleton forces in the determination of cell shape and membrane budding. *Int J Mol Sci* 22(5):2348
- Moendarbary E, Charras G (2015) Cell mechanics: hydraulic cracking. *Nat Mater* 14(3):268–269
- Mogilner A, Keren K (2009) The shape of motile cells. *Curr Biol* 19(17):762–771
- Othmer H (2018) Eukaryotic cell dynamics from crawlers to swimmers. *Wiley Interdiscip Rev Comput Mol Sci* 9(1):1376
- Paul CD, Mistriotis P, Konstantopoulos K (2017) Cancer cell motility: lessons from migration in confined spaces. *Nat Rev Cancer* 17(2):131
- Pontes B, Ayala Y, Fonseca A, Romão L, Amaral R, Salgado L, Lima F, Farina M, Viana N, Moura-Neto V et al (2013) Membrane elastic properties and cell function. *PLoS ONE* 8(7):67708
- Pontes B, Monzo P, Gauthier NC (2017) Membrane tension: a challenging but universal physical parameter in cell biology. *Semin Cell Dev Biol* 71:30–41 (**Elsevier**)
- Raval J, Gozdz W (2020) Shape transformations of vesicles induced by their adhesion to flat surfaces. *ACS Omega* 5(26):16099–16105
- Renteln P (2013) Manifolds, tensors, and forms: an introduction for mathematicians and physicists. Cambridge University Press, Cambridge
- Ruprecht V, Wieser S, Callan-Jones A, Smutny M, Morita H, Sako K, Barone V, Ritsch-Marte M, Sixt M, Voituriez R et al (2015) Cortical contractility triggers a stochastic switch to fast amoeboid cell motility. *Cell* 160(4):673–685
- Salbreux G, Charras G, Paluch E (2012) Actin cortex mechanics and cellular morphogenesis. *Trends Cell Biol* 22(10):536–545
- Seifert U (1997) Configurations of fluid membranes and vesicles. *Adv Phys* 46:13–137
- Seifert U, Bendl K, Lipowsky R (1991) Shape transformations of vesicles: phase diagram for spontaneous-curvature and bilayer-coupling models. *Phys Rev A* 44:1182–1202
- Simunovic M, Prévost C, Callan-Jones A, Bassereau P (2016) Physical basis of some membrane shaping mechanisms. *Philos Trans R Soc A Math Phys Eng Sci* 374(2072):20160034
- Simunovic M, Evergren E, Golushko I, Prévost C, Renard H-F, Johannes L, McMahon HT, Lorman V, Voth GA, Bassereau P (2016) How curvature-generating proteins build scaffolds on membrane nanotubes. *Proc Natl Acad Sci* 113(40):11226–11231
- Stachowiak JC, Hayden CC, Sasaki DY (2010) Steric confinement of proteins on lipid membranes can drive curvature and tubulation. *Proc Natl Acad Sci* 107(17):7781–7786
- Stachowiak JC, Schmid EM, Ryan CJ, Ann HS, Sasaki DY, Sherman MB, Geissler PL, Fletcher DA, Hayden CC (2012) Membrane bending by protein-protein crowding. *Nat Cell Biol* 14(9):944–949
- Stotsky J, Othmer HG (2022) How surrogates for cortical forces determine cell shape. *Int J Nonlinear Mech*
- Tu Z, Ou-Yang Z (2014) Recent theoretical advances in elasticity of membranes following Helfrich's spontaneous curvature model. *Adv Coll Interface Sci* 208:66–75
- Walker S (2018) FELICITY: a Matlab/C++ toolbox for developing finite element methods and simulation modeling. *SIAM J Sci Comput* 40(2):234–257. <https://doi.org/10.1137/17M1128745>
- Wang Q, Othmer HG (2015) Computational analysis of amoeboid swimming at low reynolds number. *J Math Biol* 72:1893–1926
- Welch MD (2015) Cell migration, freshly squeezed. *Cell* 160(4):581–582
- Wu H, de Leon MAP, Othmer HG (2018) Getting in shape and swimming: the role of cortical forces and membrane heterogeneity in eukaryotic cells. *J Math Biol* 77:1–32
- Yin Y, Chen Y, Ni D, Shi H, Fan Q (2005) Shape equations and curvature bifurcations induced by inhomogeneous rigidities in cell membranes. *J Biomech* 38(7):1433–1440
- Yuan F, Alimohamadi H, Bakka B, Trementozzi AN, Day KJ, Fawzi NL, Rangamani P, Stachowiak JC (2021) Membrane bending by protein phase separation. *Proc Nat Acad Sci* 118(11):e2017435118
- Zhang H, Wessels D, Fey P, Daniels K, Chisholm RL, Soll DR (2002) Phosphorylation of the myosin regulatory light chain plays a role in motility and polarity during dictyostelium chemotaxis. *J Cell Sci* 115(Pt 8):1733–47
- Zhong-Can O, Helfrich W (1989) Bending energy of vesicle membranes: general expressions for the first, second, and third variation of the shape energy and applications to spheres and cylinders. *Phy Rev A* 39(10):5280

Zhong-Can O-Y, Helfrich W (1989) Bending energy of vesicle membranes: general expressions for the first, second, and third variation of the shape energy and applications to spheres and cylinders. *Phys Rev A* 39(10):5280

Publisher's Note Springer Nature remains neutral with regard to jurisdictional claims in published maps and institutional affiliations.

Springer Nature or its licensor (e.g. a society or other partner) holds exclusive rights to this article under a publishing agreement with the author(s) or other rightsholder(s); author self-archiving of the accepted manuscript version of this article is solely governed by the terms of such publishing agreement and applicable law.